Available online at www.sciencedirect.com
ScienceDirect
Journal of Computational Physics 225 (2007) 464–490
JOURNAL OF COMPUTATIONAL PHYSICS
www.elsevier.com/locate/jcp

A purely Lagrangian method for computing linearly-perturbed flows in spherical geometry

Stéphane Jaouen *

CEA DIF, Département Sciences de la Simulation et de l'Information, BP 12, 91680, Bruyères-le-Châtel, France

Received 17 July 2006; received in revised form 21 November 2006; accepted 13 December 2006
Available online 23 December 2006

Abstract

In many physical applications, one wishes to control the development of multi-dimensional instabilities around a one-dimensional (1D) complex flow. For predicting the growth rates of these perturbations, a general numerical approach is viable which consists in solving simultaneously the one-dimensional equations and their linearized form for three-dimensional perturbations. In Clarisse et al. [J.-M. Clarisse, S. Jaouen, P.-A. Raviart, A Godunov-type method in Lagrangian coordinates for computing linearly-perturbed planar-symmetric flows of gas dynamics, J. Comp. Phys. 198 (2004) 80–105], a class of Godunov-type schemes for planar-symmetric flows of gas dynamics has been proposed. Pursuing this effort, we extend these results to spherically symmetric flows. A new method to derive the Lagrangian perturbation equations, based on the canonical form of systems of conservation laws with zero entropy flux [B. Després, Lagrangian systems of conservation laws. Invariance properties of Lagrangian systems of conservation laws, approximate Riemann solvers and the entropy condition, Numer. Math. 89 (2001) 99–134; B. Després, C. Mazeran, Lagrangian gas dynamics in two dimensions and Lagrangian systems, Arch. Rational Mech. Anal. 178 (2005) 327–372] is also described. It leads to many advantages. First of all, many physical problems we are interested in enter this formalism (gas dynamics, two-temperature plasma equations, ideal magnetohydrodynamics, etc.) whatever is the geometry. Secondly, a class of numerical entropic schemes is available for the basic flow [11]. Last, linearizing and devising numerical schemes for the perturbed flow is straightforward. The numerical capabilities of these methods are illustrated on three test cases of increasing difficulties and we show that – due to its simplicity and its low computational cost – the Linear Perturbations Code (LPC) is a powerful tool to understand and predict the development of hydrodynamic instabilities in the linear regime.

Keywords: Gas dynamics; Lagrangian coordinates; Spherical geometry; Linearized stability; Godunov-type methods; Richtmyer–Meshkov instability; Bell–Plesset effects

1. Introduction

Many problems in fluid dynamics and plasma physics lead to stability studies of complex flows. Controlling the development (the growth rates) of instabilities is even a key point in many experiments. As an example we

* Tel.: +33 1 69 26 68 48; fax: +33 1 69 26 70 93.
E-mail address: stephane.jaouen@cea.fr

0021-9991/$ - see front matter
doi:10.1016/j.jcp.2006.12.008

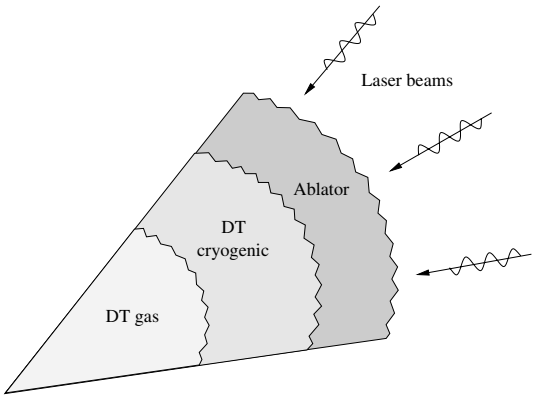

Fig. 1. Example of the direct drive laser-driven inertial confinement fusion (ICF) of a perturbed DT layered target. The unperturbed flow is spherically symmetric and we are interested in computing the time evolution of the perturbations amplitudes.

can cite the case of laser-driven Inertial Confinement Fusion [30,10], a field in which Richtmyer–Meshkov [37,32] and (ablative) Rayleigh–Taylor [36,42] instabilities have been widely studied in the last decade. In the direct drive context (Fig. 1), a spherical shell of cryogenic DT filled with gas (DT) and surrounded by an ablator (plastic) is accelerated by a direct laser irradiation. The shell is supposed to implode, compressing and heating so much the light fuel that conditions for thermonuclear burn are reached. The implosion can be presented as the succession of four different stages: the acceleration, the deceleration, the ignition and the burn phases. The mean flow is spherically symmetric, but this one-dimensional flow is unstable with respect to multi-dimensional perturbations (it is to be noticed that for planar of cylindrical targets, the phenomenology is roughly the same). Such perturbations, initially seeded by the nonuniform energy deposition and by the manufactory imperfections of the capsule itself, impose crucial limitations on symmetry and energy gain in fusion pellet implosions and can even lead to the destruction of the capsule before ignition, so that controlling the underlying mechanisms of such instabilities is a key issue for experiments designers. Indeed, the ablative Rayleigh–Taylor instability is encountered whenever density and pressure gradients are opposed ($\nabla p \cdot \nabla \rho < 0$), a situation which occurs during the acceleration phase [28,41,2] at the outer surface of the ablator, as well as during the deceleration one [39,43] at the inner shell interface. The compression of the light fuel is also achieved thanks to multiple shock reflections, so that each DT interface suffers Richtmyer–Meshkov instabilities.[1]

When dealing with such stability studies, a preliminary step consists in performing a linear stability analysis of the basic flow. Most often, such an analysis cannot be performed analytically and must be investigated numerically. Hence, there is a demand for devising efficient numerical methods for predicting linear perturbation evolutions in complex flows. When the basic flow is one-dimensional – *i.e.* planar, cylindrically or spherically symmetric – , as it is the case in ICF experiments (the above example is not limited to the spherically symmetric case), the linearized stability problem reduces to computing multi-dimensional linear perturbations about a 1D flow. This task may be achieved in a fairly inexpensive, reliable and accurate way by using 1D numerical codes for computing simultaneously the basic flow and the modal components of its linear perturbations. The underlying fluid code may either be Eulerian or Lagrangian. As it was done in [9], we shall focus on the linear Lagrangian perturbation approach which appears to be well suited for studying the linear hydrodynamic stability of interfaces, but here the case of 1D spherically symmetric basic flows, solution to the gas dynamics, is considered.

As it has been reported in a previous paper [9], this linear perturbation computation approach offers decisive advantages over multi-dimensional ones. First of all, the computational burden needed for solving the 1D equations for the basic flow and its perturbations is, at least, two (respectively four) orders of magnitude lower

[1] We refer the reader to the above references (as well as included ones) for a detailed analysis of ICF flows as well as related hydrodynamic instabilities.

than that required by standard 2D (respectively 3D) methods. Thanks to this reduced computational cost, "converged" results of linear stability problems for complex flows may be produced in a very efficient manner. Furthermore, computing linear perturbations avoids the accuracy limitations faced by 2D/3D computations when dealing with perturbations of small relative amplitudes (see the recent work of Zalesak et al. [49]). In the meantime, this approach is restricted to single mode linearized stability analysis. Therefore, the mode coupling, the saturation and the nonlinear stages can not be performed with such a tool and we are led to use direct simulations or other models. It is to be noticed that even for such studies, precise and converged single mode results may be useful. Indeed, models used to predict the evolution of multi-mode perturbations in the nonlinear stage are often based on the single mode growth rates in the linear phase. As an example we can cite the *Haan saturation model* [20].

Linear perturbation codes (PANSY [21,31], DOC [40], MV [8,19], PERTUS [7],...) have been developed in the 70s. They were all based on linearized vNR-type schemes [38]. Recently, this linear perturbation computation approach has been considered within the framework of nonlinear hyperbolic systems of conservation laws [15,16,18,24,35]. In particular, Godunov-type schemes based on a linearization of the Roe method in Lagrangian coordinates [34] have been proposed and have produced convincing results for single fluid flows of gas dynamics and of magnetohydrodynamics [35]. In [9] multi-material schemes have been proposed for planar-symmetric flows.

Pursuing this effort, we extend these results to spherically symmetric flows. Furthermore, a new method to derive the Lagrangian perturbation equations, based on the canonical form of systems of conservation laws with zero entropy flux [11,12], is also described. Using this method leads to many advantages. First of all, many physical problems we are interested in enter this formalism (gas dynamics, two-temperature plasma equations [25], ideal magnetohydrodynamics [3], etc.) whatever is the geometry. Secondly, a class of numerical entropic schemes is available for the basic flow [11]. Last, linearizing and devising numerical schemes for the perturbed flow is straightforward.

The plan of the present paper is as follows. In Section 2 we formally extend the two-dimensional Lagrangian formulation of the gas dynamics equations described in [12] in three dimensions and in spherical coordinates. Next, the obtained system is linearized about a 1D spherically symmetric flow. Thanks to a spherical harmonics decomposition, we show that the multi-dimensional linear perturbations are solution to an inhomogeneous system of 1D linear conservation laws. Numerical schemes to compute the basic and the linearized flows are described in Section 3. Numerical results on three different test cases are proposed in Section 4. We present in Section 4.1 an academic study which consists in a 1D perturbation of the interface of a shock tube test case (Sod). Results of the Linear Perturbations Code (LPC) are compared to those obtained with a Direct Method (DM), which is quite simple to implement in one dimension. In Section 4.2, interfaces are initially tri-dimensionaly perturbed. This test case consists in the study of the linear stability of an imploding shell (converging cumulative flow [27,5]) for which analytical solutions are available (smooth isentropic flow). In Section 4.3, we perform a numerical study of the Richtmyer–Meshkov instability in spherical geometry. For this test case no analytical solution is available, and results are compared to those obtained with the 2D AMR Eulerian code Hera [26]. Contrarily to the planar case, we recover the fact that the growth factor is no longer linear: when the perturbed interface undergoes geometrical convergence the perturbation growth is modified. We thus recover well-known modifications, usually referred as Bell–Plesset effects [14].

2. Lagrangian linear perturbations for the gas dynamics equations in spherical coordinates

Within the framework of continuum mechanics, an inviscid fluid is solution to the following system

$$\begin{cases} \partial_t \rho + \nabla \cdot (\rho \mathbf{u}) = 0, \\ \partial_t (\rho \mathbf{u}) + \nabla \cdot (\rho \mathbf{u} \otimes \mathbf{u}) + \nabla p = \mathbf{0}, \\ \partial_t (\rho e) + \nabla \cdot (\rho e \mathbf{u} + p \mathbf{u}) = 0, \end{cases} \tag{1}$$

where ρ is the mass density, $\mathbf{u}$ the velocity, e the total specific energy and p the pressure. For subsequent developments, we also introduce the specific volume $\tau = \frac{1}{\rho}$. This system is closed with an arbitrary equation of state

which gives the specific internal energy $\varepsilon = \varepsilon(\tau, S) = e - \frac{1}{2}\|\mathbf{u}\|^2$ as a function of the specific volume and entropy S. This closure satisfies the Gibbs relation

$$T\,\mathrm{d}S = \mathrm{d}\varepsilon + p\,\mathrm{d}\tau, \tag{2}$$

which defines the pressure and the temperature T.

2.1. Multi-dimensional Lagrangian formulation of the problem

The aim of this section is to rewrite the multi-dimensional Eulerian system (1) in Lagrangian spherical coordinates. First of all we define the coordinates change and notations that will be used in the sequel. Then we consider an arbitrary conservation law written in Eulerian coordinates and look for its equivalent in Lagrangian coordinates (see Proposition 1). This result is finally applied to the complete system (1) considered here (see Proposition 2).

2.1.1. Lagrangian spherical coordinates

Let (t, r, θ, ϕ) denote the classical spatiotemporal Eulerian coordinate system, in the spherical basis $(\mathbf{e_r}, \mathbf{e}_\theta, \mathbf{e}_\phi)$ and let $\mathbf{u} = (u_r, u_\theta, u_\phi)^t$ denote the velocity vector components. The spatiotemporal Lagrangian spherical coordinate system (t, R, Θ, Φ), which we will denote by "Lag" for shortened notations, is defined by the following fluid flow map

$$\begin{cases} \mathrm{d}t = \mathrm{d}t, \\ \mathrm{d}r = u_r\,\mathrm{d}t + A\,\mathrm{d}R + E\,\mathrm{d}\Theta + L\,\mathrm{d}\Phi, \\ \mathrm{d}\theta = \frac{u_\theta}{r}\,\mathrm{d}t + B\,\mathrm{d}R + F\,\mathrm{d}\Theta + M\,\mathrm{d}\Phi, \\ \mathrm{d}\phi = \frac{u_\phi}{r\sin\theta}\,\mathrm{d}t + C\,\mathrm{d}R + G\,\mathrm{d}\Theta + N\,\mathrm{d}\Phi. \end{cases} \tag{3}$$

For subsequent developments we also define

$$\mathbf{v} = \left(u_r, \frac{u_\theta}{r}, \frac{u_\phi}{r\sin\theta}\right)^t. \tag{4}$$

The jacobian matrix T of this coordinates change therefore reads

$$T = \begin{pmatrix} 1 & \mathbf{0}^t \\ \mathbf{v} & J \end{pmatrix} \quad \text{where } J = \frac{\partial(r,\theta,\phi)}{\partial(R,\Theta,\Phi)} = \begin{pmatrix} A & E & L \\ B & F & M \\ C & G & N \end{pmatrix}. \tag{5}$$

The determinant of J reads

$$|J| = A(FN - MG) - B(EN - LG) + C(EM - FL), \tag{6}$$

but a more practical expression of this jacobian is also available. Indeed, on an elementary volume, the mass conservation equation $\partial_t\rho + \nabla\cdot(\rho\mathbf{u}) = 0$, can be rewritten

$$\rho(0, Lag)R^2\sin\Theta\,\mathrm{d}R\,\mathrm{d}\Theta\,\mathrm{d}\Phi = \rho(t, r(t, Lag), \theta(t, Lag), \phi(t, Lag))r^2\sin\theta\,\mathrm{d}r\,\mathrm{d}\theta\,\mathrm{d}\phi.$$

Thanks to this relation, we also have

$$|J| = \det\left(\frac{\partial(r,\theta,\phi)}{\partial(R,\Theta,\Phi)}\right) = \frac{\rho(0, Lag)R^2\sin\Theta}{\rho(t, r(t, Lag), \theta(t, Lag), \phi(t, Lag))r^2\sin\theta}. \tag{7}$$

This relation will be used in the sequel. Also of interest is the comatrix of J, denoted $\tilde{J}$, which is given by

$$\tilde{J} = \begin{pmatrix} (FN - MG) & -(BN - CM) & (BG - CF) \\ -(EN - LG) & (AN - CL) & -(AG - EC) \\ (EM - FL) & -(AM - BL) & (AF - BE) \end{pmatrix}. \tag{8}$$

The fluid particle trajectories satisfy

$$\begin{cases} \partial_t r = u_r, \\ \partial_t \theta = \frac{u_\theta}{r}, \\ \partial_t \phi = \frac{u_\phi}{r \sin\theta}, \end{cases} \quad \text{together with } (r,\theta,\phi)_{|t=0} = (R,\Theta,\Phi). \tag{9}$$

2.1.2. Lagrangian form of an arbitrary Eulerian conservation law

We are now looking for the equivalent form, in the (t,R,Θ,Φ) coordinates, of the following Eulerian conservation law:

$$\partial_t a + \nabla_{(r,\theta,\phi)} \cdot \mathbf{f} = s. \tag{10}$$

The result is given in Proposition 1.

Proposition 1. *Let a, $\mathbf{f}$ and s be functions of (t,r,θ,ϕ) and assume that the Eulerian conservation law (10) holds. Then*

$$\partial_{t_{|_{R,\Theta,\Phi}}}(|J|a) + \nabla_{(R,\Theta,\Phi)} \cdot (\tilde{J}^t(\mathbf{f} - a\mathbf{v})) = |J|s, \tag{11}$$

where $|J|$, $\tilde{J}$ and $\mathbf{v}$ are respectively defined by (7), (8) and (4).

The proof, which only uses the chain rule, is proposed in Appendix A.1.

2.1.3. Application to the gas dynamics system

The developed form of the system (1) in spherical coordinates reads

$$\partial_t(r^2 \sin\theta . V) + \partial_r(r^2 \sin\theta . F(V)) + \partial_\theta(r \sin\theta . G(V)) + \partial_\phi(r . H(V)) = S(V), \tag{12a}$$

$$\text{where } \begin{cases} V = (\rho, \rho u_r, \rho u_\theta, \rho u_\phi, \rho e)^t, \\ F(V) = (\rho u_r, \rho u_r^2 + p, \rho u_r u_\theta, \rho u_r u_\phi, (\rho e + p)u_r)^t, \\ G(V) = (\rho u_\theta, \rho u_r u_\theta, \rho u_\theta^2 + p, \rho u_\theta u_\phi, (\rho e + p)u_\theta)^t, \\ H(V) = (\rho u_\phi, \rho u_r u_\phi, \rho u_\theta u_\phi, \rho u_\phi^2 + p, (\rho e + p)u_\phi)^t, \\ S(V) = (0, s_r, s_\theta, s_\phi, 0)^t, \end{cases} \tag{12b}$$

$$\text{and } \begin{cases} s_r = 2pr \sin\theta + \rho r \sin\theta (u_\theta^2 + u_\phi^2), \\ s_\theta = pr\cos\theta + \rho r(u_\phi^2 \cos\theta - u_r u_\theta \sin\theta), \\ s_\phi = -\rho r(u_\theta u_\phi \cos\theta + u_r u_\phi \sin\theta). \end{cases} \tag{12c}$$

To write the Lagrangian complete system, it is also convenient to introduce the following matrix

$$\mathcal{N} = \begin{pmatrix} 0 & 0 & 0 & 0 \\ 2r\sin\theta & 0 & -r\sin\theta \cdot \rho u_\theta & -r\sin\theta \cdot \rho u_\phi \\ r\cos\theta & r\sin\theta \cdot \rho u_\theta & 0 & -r\cos\theta \cdot \rho u_\phi \\ 0 & r\sin\theta \cdot \rho u_\phi & r\cos\theta \cdot \rho u_\phi & 0 \end{pmatrix}. \tag{13}$$

Proposition 2. *Using the conventional notation $(R,\Theta,\Phi) = (1,2,3)$, the Lagrangian formulation of the gas dynamics equations in spherical coordinates (12a)–(12c) reads*

$$\rho_0 R^2 \sin\Theta \partial_t U + \sum_{i=1}^{3} \partial_i \begin{pmatrix} \mathcal{M}_i \Psi \\ -\frac{1}{2}(\Psi, \mathcal{M}_i \Psi) \end{pmatrix} - |J| \begin{pmatrix} \mathcal{N}\Psi \\ 0 \end{pmatrix} = 0, \tag{14}$$

where $U = (\tau, u_r, u_\theta, u_\phi, e)^t$ and $\Psi = (p, -u_r, -u_\theta, -u_\phi)^t$, the symmetric matrices $\mathcal{M}_i$ being given by

$$\mathscr{M}_i = \begin{pmatrix} 0 & r^2\sin\theta\tilde{J}_{i1} & r\sin\theta\tilde{J}_{i2} & r\tilde{J}_{i3} \\ r^2\sin\theta\tilde{J}_{i1} & 0 & 0 & 0 \\ r\sin\theta\tilde{J}_{i2} & 0 & 0 & 0 \\ r\tilde{J}_{i3} & 0 & 0 & 0 \end{pmatrix},$$

where $\tilde{J}$ is the comatrix of J given by (8). Moreover, with previous notations, we have

$$\sum_{i=1}^{3} \partial_i \mathscr{M}_i - |J|(\mathscr{N} + \mathscr{N}^t) = 0. \tag{15}$$

The proof of this result is given in Appendices A.2 and A.3. System (9) must be added to complete the Lagrangian formulation.

Remark 1. The derivation of the gas dynamics Lagrangian equations has been done previously in the cartesian framework in [23,22]. Here, system (14) is written under the canonical form of Lagrangian systems with zero entropy flux and is in fact the extension in three dimensions and in the spherical coordinates system of [11,12]. The main feature of such a formalism is that, for a system of $p+1$ conservation laws, fluxes are expressed through matrix-vector products $\mathscr{M}_i\Psi$, the $p \times p$ matrices $\mathscr{M}_i$ being symmetric and independent of the physical variables.[2] When devising numerical schemes it is therefore sufficient to study these $p \times p$ matrices which reveals to be quite simpler than studying the $(p+1)\times(p+1)$ nonconstant jacobian matrices of the fluxes (we refer the reader to [11] where the derivation of a class of numerical entropic schemes is developed in a general context). Moreover, since this formalism applies to more complex systems (such as multi-dimensional two-temperature plasma equations [25] as well as ideal magnetohydrodynamics [3] for instance), the methodology described here in the context of Lagrangian linear perturbations will also apply to these models.

2.2. Lagrangian linear perturbations

For a long time, this multi-dimensional Lagrangian formalism was not used, and Lagrangian systems were written as nonconservative PDEs with Eulerian differential operators. Linearizing such a system reveals to be quite tricky (see [15,35,16,18,9]). Here, contrarily to those previous works, this can be done quite easily because spatial partial derivatives are taken over fixed Lagrangian coordinates.

Let us define $\boldsymbol{\xi} = (r,\theta,\phi)^t$, and denote by U_0 the initial value for the system (14), that is to say $U(0;R,\Theta,\Phi) = U_0(R,\Theta,\Phi)$.

Let U^0 and $\boldsymbol{\xi}^0 = (r^0,\theta^0,\phi^0)^t$ be respectively solution to (14) and (9) together with the initial conditions U_0^0 and $\boldsymbol{\xi}_0^0 = (R,\Theta,\Phi)^t$. The pair $(U^0,\boldsymbol{\xi}^0)$ is called hereafter the *basic solution* to the Lagrangian gas dynamics equations in spherical coordinates. Now we want to study its linear stability with respect to perturbations of the initial data. To do so we have to derive the linearized equations for the first order perturbations $(U^1,\boldsymbol{\xi}^1)$ of the basic solution. These are obtained in the following standard way: let ε be a small parameter. We write

$$\begin{cases} U = U^0 + \varepsilon U^1 + \cdots, \\ \boldsymbol{\xi} = \boldsymbol{\xi}^0 + \varepsilon\boldsymbol{\xi}^1 + \cdots, \end{cases}$$

and we look for the first order terms in ε in systems (14) and (9).

After straightforward calculations, we get that U^1 is solution to

$$\rho_0^1 R^2\sin\Theta\partial_t U^0 + \rho_0^0 R^2\sin\Theta\partial_t U^1 + \sum_{i=1}^{3}\partial_i\begin{pmatrix} (\mathscr{M}_i\Psi)^1 \\ -\frac{1}{2}(\Psi,\mathscr{M}_i\Psi)^1 \end{pmatrix} - |J|^0\begin{pmatrix} (\mathscr{N}\Psi)^1 \\ 0 \end{pmatrix} - |J|^1\begin{pmatrix} (\mathscr{N}\Psi)^0 \\ 0 \end{pmatrix} = 0, \tag{16}$$

[2] In the one-dimensional cartesian frame these matrices are even proved to be constant [11].

while $\boldsymbol{\xi}^1 = (r^1, \theta^1, \phi^1)^t$ is solution to

$$\begin{cases} \partial_t r^1 = u_r^1, \\ r^0 \partial_t \theta^1 + r^1 \partial_t \theta^0 = u_\theta^1, \\ r^0 \sin\theta^0 \partial_t \phi^1 + (r^1 \sin\theta^0 + r^0 \theta^1 \cos\theta^0)\partial_t \phi^0 = u_\phi^1. \end{cases} \tag{17}$$

In (16), it just remains to linearize matrix–vector products and scalar products: $(\mathscr{M}\Psi)^1 = \mathscr{M}^0\Psi^1 + \mathscr{M}^1\Psi^0$ and $(\Psi, \mathscr{M}\Psi)^1 = (\Psi^0, \mathscr{M}^1\Psi^0) + 2(\Psi^1, \mathscr{M}^0\Psi^0)$.

In addition, we have the linearized version of the divergence constraint (15) which reads

$$\sum_{i=1}^{3} \partial_i \mathscr{M}_i^1 - |J|^1(\mathscr{N} + \mathscr{N}^t)^0 - |J|^0(\mathscr{N} + \mathscr{N}^t)^1 = 0. \tag{18}$$

2.3. Application to a 1D spherically symmetric basic flow

From now on, we apply these results to the case of a 1D spherically symmetric basic flow and we assume that the basic motion is radial, so that $\mathbf{u}^0 = u_r^0 \vec{e}_r$. From (9) we therefore get $\theta^0 = \Theta$ and $\phi^0 = \Phi$. From now on, U and Ψ will be defined by

$$U = (\tau, u_r, e)^t \quad \text{and} \quad \Psi = (p, -u_r)^t.$$

2.3.1. Lagrangian equations for the basic flow

At zeroth order, the jacobian matrix simply reads

$$J^0 = \begin{pmatrix} A^0 & 0 & 0 \\ 0 & 1 & 0 \\ 0 & 0 & 1 \end{pmatrix} \quad \text{with } A^0 = \partial_R r^0 = \frac{\rho_0^0 R^2}{\rho^0 (r^0)^2}, \tag{19}$$

where (7) has been used to express A^0. It means that $B^0 = C^0 = E^0 = G^0 = L^0 = M^0 = 0$ and $F^0 = N^0 = 1$. Thanks to these simplifications on the components of the jacobian matrix, we get that the basic flow solves

$$\begin{cases} \partial_t U^0 + \partial_m \begin{pmatrix} (r^0)^2 \mathscr{C}\Psi^0 \\ -\frac{1}{2}(r^0)^2 (\Psi^0, \mathscr{C}\Psi^0) \end{pmatrix} = S^0, \\ \partial_t r^0 = u_r^0, \end{cases} \tag{20a}$$

where the matrix $\mathscr{C}$ and the vector S are defined by

$$\mathscr{C} = \begin{pmatrix} 0 & 1 \\ 1 & 0 \end{pmatrix} \quad \text{and} \quad S = (0, p\partial_m r^2, 0)^t. \tag{20b}$$

In (20a), we have introduced the mass variable m, defined by $\mathrm{d}m = \rho_0^0 R^2 \,\mathrm{d}R = \rho^0 (r^0)^2 \,\mathrm{d}r$.

2.3.2. Lagrangian equations for the linearized flow

Before giving the systems satisfied by the linear perturbations about this 1D basic flow, we detail how simplifications occur on the first equation of (16), that is on the perturbed specific volume. From (16), and using simplifications due to (19), the developed form of this equation reads

$$\begin{aligned} &\rho_0^0 R^2 \sin\Theta \partial_t \tau^1 + \rho_0^1 R^2 \sin\Theta \partial_t \tau^0 - \partial_R (r^2 \sin\theta \cdot u_r)^1 - \partial_R ((F^1 + N^1)(r^2 \sin\theta \cdot u_r)^0) + \partial_\Theta (B^1 (r^2 \sin\theta \cdot u_r)^0) \\ &\quad + \partial_\Phi (C^1 (r^2 \sin\theta \cdot u_r)^0) - \partial_\Theta (A^0 r^0 \sin\theta^0 \cdot u_\theta^1) - \partial_\Phi (A^0 r^0 \cdot u_\phi^1) = 0. \end{aligned}$$

But we have $\partial_R(F^1 + N^1) - \partial_\Theta B^1 - \partial_\Phi C^1 = 0$ which is a consequence of the linearized divergence constraint (18). Using this property and the fact that the basic flow does not depend on $\Theta = \theta^0$ and $\Phi = \phi^0$, we get

$$\rho_0^0 R^2 \partial_t \tau^1 + \rho_0^1 R^2 \partial_t \tau^0 - \partial_R (r^2 u_r)^1 - \left(F^1 + N^1 + \theta^1 \frac{\cos \Theta}{\sin \Theta} \right) \partial_R (r^2 u_r)^0 - \frac{r^0 A^0}{\sin \Theta} (\partial_\Theta (\sin \Theta \cdot u_\theta^1) + \partial_\Phi u_\phi^1) = 0. \tag{21}$$

Then we introduce the following transverse operators

$$\nabla_\perp \cdot (f_\Theta, f_\Phi)^t = \frac{1}{r^0 \sin \Theta} (\partial_\Theta (f_\Theta \sin \Theta) + \partial_\Phi f_\Phi), \tag{22a}$$

$$\Delta_\perp \lambda = \frac{1}{\sin \Theta} \left(\partial_\Theta (\sin \Theta \partial_\Theta \lambda) + \frac{1}{\sin \Theta} \partial^2_{\Phi\Phi} \lambda \right), \tag{22b}$$

and define the transverse dilatation Λ^1 (which is the transverse divergence of the linearized displacement), and Ω^1, its temporal derivative:

$$\Lambda^1 = \nabla_\perp \cdot (r^0 \theta^1, r^0 \sin \Theta \phi^1)^t, \tag{23a}$$

$$\Omega^1 = \partial_t \Lambda^1 = \nabla_\perp \cdot (u_\theta^1, u_\phi^1)^t. \tag{23b}$$

With these notations, one can easily check that

$$\Lambda^1 = \frac{1}{\sin \Theta} (\theta^1 \cos \Theta + \sin \Theta (F^1 + N^1)). \tag{24}$$

Eq. (21) rewrites

$$\rho_0^0 R^2 \partial_t \tau^1 + \rho_0^1 R^2 \partial_t \tau^0 - \partial_R (r^2 u_r)^1 - \Lambda^1 \partial_R (r^2 u_r)^0 - (r^0)^2 A^0 \Omega^1 = 0,$$

that is to say

$$\partial_t \tau^1 + \frac{\rho_0^1}{\rho_0^0} \partial_t \tau^0 - \partial_m (r^2 u_r)^1 = \Lambda^1 \partial_m (r^2 u_r)^0 + \tau^0 \Omega^1. \tag{25}$$

This kind of calculation can be done on each component of the system. Finally, setting

$$\mathscr{F}(U) = \begin{pmatrix} r^2 \mathscr{C} \Psi \\ -\frac{1}{2} r^2 (\Psi, \mathscr{C} \Psi) \end{pmatrix}, \tag{26}$$

we find that $(U^1, r^1, \Lambda^1, \Omega^1)$ solves

$$\begin{cases} \partial_t U^1 + \frac{\rho_0^1}{\rho_0^0} \partial_t U^0 + \partial_m \mathscr{F}^1 + \Lambda^1 \partial_m \mathscr{F}^0 = \Sigma, \\ \partial_t r^1 = u_r^1, \\ \partial_t \Lambda^1 = \Omega^1, \\ \partial_t ((r^0)^2 \Omega^1) = -\tau^0 \Delta_\perp p^1 + (r^0)^2 \partial_m p^0 \cdot \Delta_\perp r^1, \end{cases} \tag{27a}$$

with Σ given by

$$\Sigma = S^0 \Lambda^1 + S^1 + (\tau^0 \Omega^1, 0, -\tau^0 p^0 \Omega^1)^t, \tag{27b}$$

the vector S being defined by (20b).

Note that since $\mathscr{C}$ is a constant symmetric matrix, we simply have

$$\partial_m \mathscr{F}^1 = \partial_m \begin{pmatrix} (r^0)^2 \mathscr{C} \Psi^1 + 2 r^0 r^1 \mathscr{C} \Psi^0 \\ -(r^0)^2 (\Psi^0, \mathscr{C} \Psi^1) - r^0 r^1 (\Psi^0, \mathscr{C} \Psi^0) \end{pmatrix}.$$

Remark 2. A first integral on the linearized equation of the specific volume (25) is also available. After straightforward manipulations, this equation can be rewritten

$$\partial_t\left(\tau^1+\frac{\rho_0^1}{\rho_0^0}\tau^0-\partial_m((r^0)^2r^1)-\tau^0\Lambda^1\right)=0, \tag{28}$$

so that this quantity is constant in time. In fact we have

$$\tau^1+\frac{\rho_0^1}{\rho_0^0}\tau^0-\partial_m((r^0)^2r^1)-\tau^0\Lambda^1=0. \tag{29}$$

This is due to the choice of the Lagrangian coordinates. At $t=0$, we have $|J|^0=1$ and $|J|^1=0$. Linearizing (7) gives

$$\left[\frac{\rho_0^1}{\rho_0^0}-\frac{\rho^1}{\rho^0}-\frac{2r^0r^1}{(r^0)^2}-\theta^1P\cot g\theta^0\right]_{t=0}=0,$$

which rewrites, multiplying by τ^0 and using (24),

$$\left[\tau^1-\frac{\rho_0^1}{\rho_0^0}\tau^0-\partial_m((r^0)^2r^1)-\Lambda^1\tau^0+\frac{\tau^0}{A^0}(A^1+A^0(F^1+N^1))\right]_{t=0}=0.$$

Linearizing (6) immediately gives $A^1+A^0(F^1+N^1)=0$ at $t=0$, so that (29) holds.

The linearized flow is therefore solution to the tridimensional equations (27a) and (27b). This kind of system may then be reduced to a 1D system for the modal components of the linear perturbations. To achieve this task, we introduce the spherical harmonics basis.

2.3.3. Spherical harmonics decomposition

Let us denote $P_{l,m}$ the spherical harmonics basis of degree l and order m. Any linearized quantity f^1 is therefore developed in the following way

$$f^1(t;R,\Theta,\Phi)=\sum_{l=0}^{\infty}\sum_{m=-l}^{m=l}\tilde{f}_{l,m}(t;R)P_{l,m}(\Theta,\Phi),$$

and we have

$$\Delta_\perp P_{l,m}=-l(l+1)P_{l,m}. \tag{30}$$

From now on, we omit the exponent relative to the basic flow, and indices relative to the modal components. Using (30), it is then a simple matter to check that the modal component of degree l is solution to

$$\begin{cases}\partial_t\tilde{U}+\frac{\tilde{\rho}_0}{\rho_0}\partial_tU+\partial_m\tilde{\mathscr{F}}+\tilde{\Lambda}\partial_m\mathscr{F}=\tilde{\Sigma},\\ \partial_t\tilde{r}=\tilde{u}_r,\\ \partial_t\tilde{\Lambda}=\tilde{\Omega},\\ \partial_t(r^2\tilde{\Omega})=\omega[\tau\tilde{p}-r^2\tilde{r}\partial_mp],\end{cases} \tag{31a}$$

where $\omega=l(l+1)$ and

$$\tilde{\Sigma}=S\tilde{\Lambda}+\tilde{S}+(\tau\tilde{\Omega},0,-\tau p\tilde{\Omega})^t. \tag{31b}$$

Therefore, the modal component of degree l is solution to an inhomogenous 1D system. Investigating the linearized stability of the basic solution (U,r) with respect to longitudinal and transverse perturbations amounts to solve the system (31a) and (31b) for various relevant modes l and to study the asymptotic behavior in time of the corresponding solutions.

3. Numerical schemes

We propose in this section to derive numerical schemes for computing simultaneously the basic and the linearized flows solution to (20a) and (20b) and (31a) and (31b). Introducing the geometrical parameter $\mathscr{A}=r^2$, its linearized expression $\tilde{\mathscr{A}}=2r\tilde{r}$ and rewriting the flux $\mathscr{F}=\mathscr{A}F$ with

$$F = \begin{pmatrix} \mathscr{C}\Psi \\ -\frac{1}{2}(\Psi, \mathscr{C}\Psi) \end{pmatrix}, \tag{32}$$

it is found that these systems read

1. Basic flow:

$$\partial_t U + \partial_m(\mathscr{A}F) = S, \tag{33a}$$
$$\partial_t r = u_r. \tag{33b}$$

2. Linearized flow:

$$\partial_t \tilde{U} + \frac{\tilde{\rho}_0}{\rho_0}\partial_t U + \partial_m(\mathscr{A}\tilde{F} + \tilde{\mathscr{A}}F) + \tilde{\Lambda}\partial_m(\mathscr{A}F) = \tilde{\Sigma}, \tag{33c}$$
$$\partial_t \tilde{r} = \tilde{u}_r, \tag{33d}$$
$$\partial_t \tilde{\Lambda} = \tilde{\Omega}, \tag{33e}$$
$$\partial_t(\mathscr{A}\tilde{\Omega}) = \omega[\tau\tilde{p} - \mathscr{A}\tilde{r}\partial_m p], \tag{33f}$$

with $S = (0, p\partial_m\mathscr{A}, 0)^t$ and $\tilde{\Sigma} = S\tilde{\Lambda} + \tilde{S} + (\tau\tilde{\Omega}, 0, -\tau p\tilde{\Omega})^t$.

The interest of introducing the geometrical parameter $\mathscr{A}$ lies in the following:

Remark 3. It can be shown that these equations are exactly those one obtain for a planar-symmetric basic flow, setting in that case $\omega = k^2$ where k is the Fourier mode number, $\mathscr{A} = 1$ and $\tilde{\mathscr{A}} = 0$ (see [9]). Using these notations allows us to treat both cases in a generic way. Therefore, numerical schemes described in the following sections will apply to both cases, with slight simplifications in the latter one.

The 1D domain $[R_{\min}, R_{\max}]$ is discretized in N cells $I_j = [R_{j-\frac{1}{2}}, R_{j+\frac{1}{2}}]$, with $R_{\frac{1}{2}} = R_{\min}$ and $R_{N+\frac{1}{2}} = R_{\max}$. The mass coordinates are therefore given by

$$\begin{cases} m_{\frac{1}{2}} = 0, \\ m_{j+\frac{1}{2}} = m_{j-\frac{1}{2}} + \Delta m_j, \quad \text{for } j = 2, \ldots, N, \end{cases}$$

with $\Delta m_j = \int_{R_{j-\frac{1}{2}}}^{R_{j+\frac{1}{2}}} \rho_0 \mathscr{A}\,\mathrm{d}r$, that is to say

$$\Delta m_j = \begin{cases} \rho_{0,j}\Delta R_j & \text{in the planar case,} \\ \rho_{0,j}\frac{R_{j+\frac{1}{2}}^2 + R_{j+\frac{1}{2}}R_{j-\frac{1}{2}} + R_{j-\frac{1}{2}}^2}{3}\Delta R_j & \text{in the spherical case.} \end{cases} \tag{34}$$

Given a mesh size Δm_j and a time step Δt, we define an approximation U_j^n of $U(m_j, t^n)$ at the point (m_j, t^n):

$$U_j^n = \frac{1}{\Delta m_j}\int_{m_{j-\frac{1}{2}}}^{m_{j+\frac{1}{2}}} U(m, t^n)\mathrm{d}m. \tag{35}$$

3.1. Numerical scheme for the basic flow

We focus here on the discretization of (33a) and (33b). The explicit Godunov-type scheme takes the following form:

$$U_j^{n+1} = U_j^n - \frac{\Delta t}{\Delta m_j}\left(\mathscr{A}_{j+\frac{1}{2}}^n F(U)_{j+\frac{1}{2}}^n - \mathscr{A}_{j-\frac{1}{2}}^n F(U)_{j-\frac{1}{2}}^n\right) + \Delta t S_j^n, \tag{36}$$

where $F(U)_{j+\frac{1}{2}}^n$ is the numerical flux.

Numerical flux $F(U)_{j+\frac{1}{2}}^n$. Since F is given by (32), with $\mathscr{C}$ a symmetric constant matrix, we see that having determined $\Psi_{j+\frac{1}{2}}^* = (p_{j+\frac{1}{2}}^*, -u_{j+\frac{1}{2}}^*)^t$ the last component of the flux $-\frac{1}{2}(\Psi, \mathscr{C}\Psi)_{j+\frac{1}{2}}^* = p_{j+\frac{1}{2}}^* u_{j+\frac{1}{2}}^*$ is known.

To compute $u^*_{j+\frac{1}{2}}$ and $p^*_{j+\frac{1}{2}}$ an approximate Riemann solver is used. A classical way to proceed is to use the linearized Riemann invariants. Indeed, along the characteristic curves $C_\pm$ defined by $\mathrm{d}m = \pm(\rho c)\,\mathrm{d}t$, where (ρc) is the Lagrangian speed of sound, we have $\mathrm{d}p \pm (\rho c)\,\mathrm{d}p = 0$ (see [1,17]) so that integration on these curves leads to

$$\begin{cases} (p^*_{j+\frac{1}{2}} - p_j) + (\rho c)_j (u^*_{j+\frac{1}{2}} - u_j) = 0 & \text{along } C^+ \text{ coming from the cell } I_j, \\ (p^*_{j+\frac{1}{2}} - p_{j+1}) - (\rho c)_{j+1} (u^*_{j+\frac{1}{2}} - u_{j+1}) = 0 & \text{along } C^- \text{ coming from the cell } I_{j+1}. \end{cases}$$

Therefore,

$$\begin{cases} p^*_{j+\frac{1}{2}} = \frac{(\rho c)_j p_{j+1} + (\rho c)_{j+1} p_j}{(\rho c)_j + (\rho c)_{j+1}} + \frac{(\rho c)_j (\rho c)_{j+1}}{(\rho c)_j + (\rho c)_{j+1}} (u_j - u_{j+1}), \\ u^*_{j+\frac{1}{2}} = \frac{(\rho c)_j u_j + (\rho c)_{j+1} u_{j+1}}{(\rho c)_j + (\rho c)_{j+1}} + \frac{1}{(\rho c)_j + (\rho c)_{j+1}} (p_j - p_{j+1}), \end{cases} \tag{37}$$

which is the well-known Godunov acoustic Riemann solver. It is proved in [12] that the Godunov scheme together with the acoustic Riemann solver (37) is entropic under the CFL condition

$$\max_j (\rho c)_j \frac{\Delta t}{\Delta m_j} \leqslant 1. \tag{38}$$

Having defined the velocities of interfaces, Eq. (33b) is discretized in the following way:

$$r^{n+1}_{j+\frac{1}{2}} = r^n_{j+\frac{1}{2}} + \Delta t u^*_{j+\frac{1}{2}}. \tag{39}$$

Geometrical parameter $\mathscr{A}^n_{j+\frac{1}{2}}$. Since we wish the equation on the specific volume to be equivalent at the discrete level to the mass conservation

$$\rho^{n+1}_j (V_{j+\frac{1}{2}} - V_{j-\frac{1}{2}})^{n+1} = \rho^n_j (V_{j+\frac{1}{2}} - V_{j-\frac{1}{2}})^n, \tag{40}$$

its discretization is imposed. Indeed, we have the following:

Lemma 1. *Let*

$$\mathscr{A}^n_{j+\frac{1}{2}} = 1 \text{ in the planar case}, \tag{41a}$$

$$\mathscr{A}^n_{j+\frac{1}{2}} = \frac{\left(r^{n+1}_{j+\frac{1}{2}}\right)^2 + r^{n+1}_{j+\frac{1}{2}} r^n_{j+\frac{1}{2}} + \left(r^n_{j+\frac{1}{2}}\right)^2}{3} \text{ in the spherical case}. \tag{41b}$$

The scheme (36)–(41) implies the mass conservation of the basic flow at the discrete level.

The proof is quite simple. Using (39), the first equation of (36) rewrites

$$\tau^{n+1}_j = \tau^n_j + \frac{1}{\Delta m_j} \left(\mathscr{A}^n_{j+\frac{1}{2}} (r^{n+1}_{j+\frac{1}{2}} - r^n_{j+\frac{1}{2}}) - \mathscr{A}^n_{j-\frac{1}{2}} (r^{n+1}_{j-\frac{1}{2}} - r^n_{j-\frac{1}{2}}) \right),$$

so that (40) is trivially satisfied in the planar case. Inserting (41b) in this equation also leads to (40) after few manipulations.

Geometrical source term S^n_j. It remains to give the expression of S^n_j. The choice we made is motivated by the following observation: for a system initially at rest in an uniform pressure field, the velocity has to remain zero. The following choice fulfill this requirement and is commonly used:

$$S^n_j = \left(0, \frac{p^*_{j+\frac{1}{2}} + p^*_{j-\frac{1}{2}}}{2} \frac{\mathscr{A}^n_{j+\frac{1}{2}} - \mathscr{A}^n_{j-\frac{1}{2}}}{\Delta m_j}, 0 \right)^t. \tag{42}$$

3.2. Numerical scheme for the linearized flow

Now we focus on the discretization of (33c)–(33f) . Here again we use a Godunov-type scheme which is somewhat close to the one presented in [9]. To avoid additional stability constraints, transverse contributions

are implicited. This will help us to deal with high mode numbers ($\omega \gg 1$) for which source terms may become stiff. The scheme writes

$$\tilde{U}_j^{n+1} = \tilde{U}_j^n - \frac{\tilde{\rho}_{0j}}{\rho_{0_j}}\left(U_j^{n+1} - U_j^n\right) + \Delta t\tilde{\Sigma}_j^{n+1} - \frac{\Delta t}{\Delta m_j}\left(\tilde{\mathscr{A}}^n_{j+\frac{1}{2}}F(U)^n_{j+\frac{1}{2}} - \tilde{\mathscr{A}}^n_{j-\frac{1}{2}}F(U)^n_{j-\frac{1}{2}}\right)$$
$$- \frac{\Delta t}{\Delta m_j}\left(\mathscr{A}^n_{j+\frac{1}{2}}\tilde{F}(U)^n_{j+\frac{1}{2}} - \mathscr{A}^n_{j-\frac{1}{2}}\tilde{F}(U)^n_{j-\frac{1}{2}}\right) - \frac{\Delta t}{\Delta m_j}\left(\mathscr{A}^n_{j+\frac{1}{2}}F(U)^n_{j+\frac{1}{2}} - \mathscr{A}^n_{j-\frac{1}{2}}F(U)^n_{j-\frac{1}{2}}\right)\tilde{\Lambda}_j^{n+1}, \tag{43a}$$

$$\tilde{r}^{n+1}_{j+\frac{1}{2}} = \tilde{r}^n_{j+\frac{1}{2}} + \Delta t\tilde{u}^*_{j+\frac{1}{2}}, \tag{43b}$$

$$\tilde{\Lambda}_j^{n+1} = \tilde{\Lambda}_j^n + \Delta t\tilde{\Omega}_j^{n+1}, \tag{43c}$$

$$(\mathscr{A}\tilde{\Omega})_j^{n+1} = (\mathscr{A}\tilde{\Omega})_j^n + \omega\Delta t\left[(\tau\tilde{p})_j^{n+1} - \frac{(\mathscr{A}\tilde{r})^n_{j+\frac{1}{2}} + (\mathscr{A}\tilde{r})^n_{j-\frac{1}{2}}}{2}\frac{p^*_{j+\frac{1}{2}} - p^*_{j-\frac{1}{2}}}{\Delta m_j}\right]. \tag{43d}$$

Numerical flux $\tilde{F}(U)^n_{j+\frac{1}{2}}$. Since $\mathscr{C}$ is a constant matrix (see (20b)), the discrete form of the linearized flux $\tilde{F}$ is straightforward:

$$\tilde{F}(U)^n_{j+\frac{1}{2}} = \begin{pmatrix} \mathscr{C}\tilde{\Psi}^*_{j+\frac{1}{2}} \\ -(\Psi^*_{j+\frac{1}{2}})^t\mathscr{C}\tilde{\Psi}^*_{j+\frac{1}{2}} \end{pmatrix} = \begin{pmatrix} -\tilde{u}^*_{j+\frac{1}{2}} \\ \tilde{p}^*_{j+\frac{1}{2}} \\ \tilde{p}^*_{j+\frac{1}{2}}u^*_{j+\frac{1}{2}} + p^*_{j+\frac{1}{2}}\tilde{u}^*_{j+\frac{1}{2}} \end{pmatrix}, \tag{44}$$

with $\tilde{\Psi}^*_{j+\frac{1}{2}}$ given by (37), with $\tilde{u}^n_i$ and $\tilde{p}^n_i$ in place of, respectively, u^n_i and p^n_i (for $i = j, j+1$).

Geometrical parameter $\tilde{\mathscr{A}}^n_{j+\frac{1}{2}}$ and source term $\tilde{\Sigma}^{n+1}_j$. They are defined by

$$\tilde{\Sigma}_j^{n+1} = \begin{pmatrix} \tau^n_j\tilde{\Omega}^{n+1}_j \\ \tilde{S}^n_j + S^n_j\tilde{\Lambda}^{n+1}_j \\ -\tau^n_j p^{n+1}_j\tilde{\Omega}^{n+1}_j \end{pmatrix}, \tag{45}$$

and

$$\tilde{\mathscr{A}}^n_{j+\frac{1}{2}} = 0 \quad \text{in the planar case,} \tag{46a}$$

$$\tilde{\mathscr{A}}^n_{j+\frac{1}{2}} = \frac{1}{3}(2r^{n+1}\tilde{r}^{n+1} + r^{n+1}\tilde{r}^n + r^n\tilde{r}^{n+1} + 2r^n\tilde{r}^n)_{j+\frac{1}{2}} \quad \text{in the spherical case.} \tag{46b}$$

As for the basic flow, this choice is motivated by the

Lemma 2. *The scheme (43)–(46) implies the mass conservation of the linear flow (28) at the discrete level.*

This implies that if (29) is true at $t = 0$, it will be true at any time $t^n > 0$. The proof is quite simple and is not detailed here.

Remark 4. Once $\tilde{\Omega}^{n+1}_j$ is known, the discrete equations can be solved explicitly as we explain now. In order to solve (43d) we use the fundamental principle of thermodynamics (2) written in terms of the independent variables τ, e, u and p:

$$\tau\,\mathrm{d}p = (\Gamma - \gamma)p\,\mathrm{d}\tau + \Gamma\,\mathrm{d}e - \Gamma u\,\mathrm{d}p, \tag{47}$$

where γ and Γ are respectively the adiabatic exponent and the Grüneisen coefficient.[3] Therefore, omitting the $n+1$ exponent,

$$\tau\tilde{p} = (\Gamma - \gamma)p\tilde{\tau} + \Gamma\tilde{e} - \Gamma u\tilde{u}.$$

Using (43a)–(43c) it is easily shown that Eq. (43d) can be rewritten

$$(\mathscr{A}^{n+1}_j - \omega\Delta t\alpha_j)\tilde{\Omega}^{n+1}_j = (\mathscr{A}\tilde{\Omega})^n_j + \omega\Delta t\beta_j,$$

where α_j and β_j can be computed explicitly.

[3] For a perfect gas law, $\Gamma = \gamma - 1$, but numerical schemes described here apply in a more general case.

3.3. Extension to second-order accurate schemes

For increasing the order of accuracy of the above Godunov-type methods, a two steps Lax–Wendroff-type scheme [29] together with flux limiting techniques has been used. The momentum and the energy equations of the basic flow can be manipulated to give, in a nonconservative form:

$$\begin{cases} \frac{\partial u}{\partial t} + \mathscr{A}\frac{\partial p}{\partial m} = 0, \\ \frac{\partial p}{\partial t} + (\rho c)^2 \frac{\partial \mathscr{A} u}{\partial m} = 0. \end{cases}$$

A Lax–Wendroff-type scheme is applied over a half-time step $\Delta t/2$ (we refer to [1] for further details) thus giving a second-order approximation of the velocity and the pressure at each interface $m_{j+\frac{1}{2}}$, respectively, denoted $u^{*,LW}_{j+\frac{1}{2}}$ and $p^{*,LW}_{j+\frac{1}{2}}$. This solver, say $u^{*,HI}$ and $p^{*,HI}$, is connected to the first order one, $u^{*,LO}$ and $p^{*,LO}$, *via* a Van Leer flux limiter Φ (cf. [44]):

$$\begin{cases} u^{*,HI} = \Phi u^{*,LO} + (1-\Phi) u^{*,LW}, \\ p^{*,HI} = \Phi p^{*,LO} + (1-\Phi) p^{*,LW}. \end{cases} \tag{48}$$

In an extended form, the second-order accurate solver for the basic flow writes

$$\begin{cases} u^*_{j+\frac{1}{2}} = \frac{(\rho c)_j u_j + (\rho c)_{j+1} u_{j+1}}{(\rho c)_j + (\rho c)_{j+1}} + \Phi \frac{1}{(\rho c)_j + (\rho c)_{j+1}} (p^n_j - p^n_{j+1}) + (1-\Phi)\frac{\Delta t}{2} \mathscr{A}_{j+\frac{1}{2}} \frac{p^n_j - p^n_{j+1}}{m_{j+1} - m_j}, \\ p^*_{j+\frac{1}{2}} = \frac{(\rho c)_j p_{j+1} + (\rho c)_{j+1} p_j}{(\rho c)_j + (\rho c)_{j+1}} + \Phi \frac{(\rho c)_j (\rho c)_{j+1}}{(\rho c)_j + (\rho c)_{j+1}} (u^n_j - u^n_{j+1}) + (1-\Phi)\frac{\Delta t}{2} \frac{(\rho c)^2_j + (\rho c)^2_{j+1}}{2} \frac{\mathscr{A}_j u^n_j - \mathscr{A}_{j+1} u^n_{j+1}}{m_{j+1} - m_j}, \end{cases} \tag{49}$$

with $\mathscr{A} = 1$ or r^2 whether we consider the planar or the spherical geometry and

$$m_{j+1} - m_j = \begin{cases} \rho_{0,j}(R_{j+\frac{1}{2}} - R_j) + \rho_{0,j+1}(R_{j+1} - R_{j+\frac{1}{2}}) & \text{in the planar case,} \\ \rho_{0,j} \frac{R^3_{j+\frac{1}{2}} - R^3_j}{3} + \rho_{0,j+1} \frac{R^3_{j+1} - R^3_{j+\frac{1}{2}}}{3} & \text{in the spherical case.} \end{cases}$$

As for the first order accurate scheme, the time step is still given (38). Here we have chosen the Van Leer limiter (see [44]) which is defined by

$$\begin{cases} \Phi = 0 \quad \text{if } D_{j+\frac{1}{2}} \geqslant 0, \\ \Phi = 1 - \max\left[0, \min\left(1, 2\alpha_j, 2\alpha_{j+1}, \frac{\alpha_j + \alpha_{j+1}}{2}\right)\right] \quad \text{otherwise,} \end{cases} \tag{50}$$

where $\alpha_j = \frac{D_j}{D_{j+\frac{1}{2}}}$ and $\alpha_{j+1} = \frac{D_{j+1}}{D_{j+\frac{1}{2}}}$, with D_j, $D_{j+\frac{1}{2}}$ and D_{j+1} given by

$$D_{j+\frac{1}{2}} = \frac{u_{j+1} - u_j}{m_{j+1} - m_j}, \quad D_{j+1} = \frac{u_{j+\frac{3}{2}} - u_{j+\frac{1}{2}}}{\Delta m_{j+1}}, \quad D_j = \frac{u_{j+\frac{1}{2}} - u_{j-\frac{1}{2}}}{\Delta m_j}.$$

Since the linearized flow satisfies a linear system of conservation laws, we could infer that no flux limiting techniques should be necessary for computing the linear perturbation. The situation is in fact much more complex, because the perturbed flow is solution to a linear system of conservation laws with discontinuous coefficients. In practice the same limiter as for the basic flow is applied. Therefore, the second-order riemann solver for computing the linearized solution corresponds to (49) with $\tilde{u}^n_i$ and $\tilde{p}^n_i$ in place of, respectively, u^n_i and p^n_i (for $i = j, j+1$).

4. Numerical results

In order to validate this method, we compare numerical results we obtain to analytical solutions when these ones are available (Section 4.2). But most often, we are led to perform direct numerical simulations on the perturbed flow U^ε and to use a postprocessor to get back to linear perturbations. This is what is done in Sections 4.1 and 4.3.

4.1. Monodimensional perturbation

The first test case we consider (maybe the simplest) is the case of a monodimensional perturbation. Since the perturbed flow remains one dimensional, we compute separately, with two runs, the unperturbed $U(R,t)$ and the perturbed $U^\varepsilon(R,t)$ flows using the numerical scheme described in Section 3.1. Then we compare $\frac{U^\varepsilon(R,t)-U(R,t)}{\varepsilon}$ with $\tilde{U}(R,t)$ obtained with the LPC. Such a procedure is referred in the sequel as the Direct Method (DM).

Let the basic flow U be solution to the one dimensional Sod shock tube. The initial condition for U is given by $U_0(R < R_{\text{int}}) = U_l$ and $U_0(R > R_{\text{int}}) = U_r$ with $R_{\text{int}} = 0.5$ and

$$U_l = \begin{cases} \rho_l = 1, \\ u_l = 0, \\ p_l = 1, \end{cases} \quad \text{and} \quad U_r = \begin{cases} \rho_r = 0.125, \\ u_r = 0, \\ p_r = 0.1, \end{cases}$$

together with a perfect gas equation of state with $\gamma = 1.4$. Assume that the interface position is perturbed: $R^\varepsilon_{\text{int}} = R_{\text{int}} + \varepsilon$ with $\varepsilon \ll 1$ in order to stay in a linear regime. At the continuous level, we have $U^\varepsilon_0(R) = U_0(R-\varepsilon)$.

4.1.1. Initial conditions

Initial conditions for the DM. Let k be the index such that at the discrete level we have $R_{\text{int}} = R_{k-\frac{1}{2}}$ and assume that $0 < \varepsilon < R_{k+\frac{1}{2}} - R_{k-\frac{1}{2}}$ (the amplitude of the radial perturbation is smaller than the mesh size). The initial condition for the perturbed flow is discretized in the following way:

$$U^\varepsilon_{0,j\neq k} = U_{0,j} \quad \text{and} \quad U^\varepsilon_{0,k} = U_{0,k} - \varepsilon \frac{U_{0,k} - U_{0,k-1}}{R_{k+\frac{1}{2}} - R_{k-\frac{1}{2}}},$$

so that the discrete Lagrangian coordinates remain the same for the unperturbed and the perturbed flow. With such a choice the difference $\frac{U^\varepsilon(R,t)-U(R,t)}{\varepsilon}$ can easily be computed. For applications we have chosen $\varepsilon = 10^{-5}$.

Initial conditions for the LPC. The initial condition used for the LPC is simply $\tilde{U}_0(R) = 0$ and

$$\tilde{r}_{0,j-\frac{1}{2}} = \begin{cases} 1 & \text{if } j = k, \\ 0 & \text{otherwise.} \end{cases}$$

The transverse displacement field, which is linked to $\tilde{r}_0(R)$ through Eq. (29) is given by

$$\tilde{\Lambda}_{0,j} = -\rho_{0,j} \frac{(\mathscr{A}\tilde{r})_{0,j+\frac{1}{2}} - (\mathscr{A}\tilde{r})_{0,j-\frac{1}{2}}}{\Delta m_j}.$$

4.1.2. Numerical results

The domain $[0,1]$ is discretized on 1000 regular cells[4] and for both methods the second order scheme has been used. Radial perturbations ($\tilde{r}(R,t)$ for the LPC code and $\frac{r^\varepsilon(R,t)-r(R,t)}{\varepsilon}$ for the DM) for the planar and the spherical cases are respectively given in Figs. 2 and 3 at time $t = 0.25$.

Remark 5. Since the perturbed solution is just translated from ε in the planar case, we have, at the continuous level $r^\varepsilon(R+\varepsilon,t) = r^0(R,t) + \varepsilon$. On the other hand, a Taylor expansion yields $r^\varepsilon(R+\varepsilon,t) = r^\varepsilon(R,t) + \varepsilon \partial_R r^\varepsilon(R,t)$ so that, up to the first order in ε we have

$$r^\varepsilon(R,t) = r^0(R,t) + \varepsilon\left(1 - \frac{\partial r^0(R,t)}{\mathrm{d}R}\right).$$

Therefore, knowing the $r^0(R,t)$ profile allows us to compute the first order perturbation in the planar case. This one is also plotted in Fig. 2(right).

[4] The truncature error of the computed solution $U^\varepsilon - U$ has to be at least one or two order of magnitude lower than ε to give relevant results, so that a minimum of 1000 cells is required here to apply the DM.

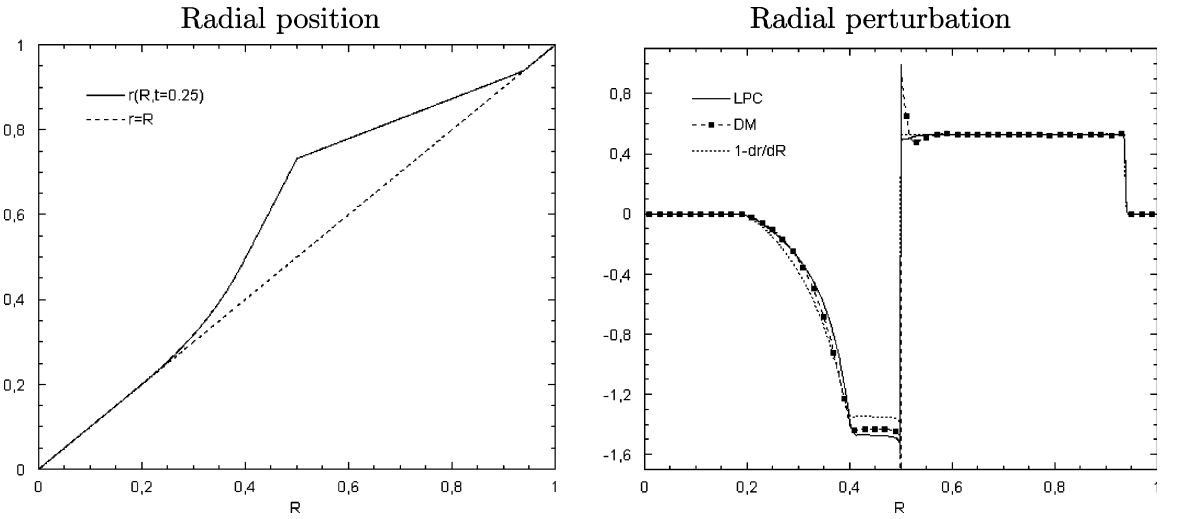

Fig. 2. Monodimensional perturbation in the planar geometry at $t = 0.25$. Left: unperturbed radial position $r(R,t)$. Right: comparison of the radial perturbation obtained with the LPC code and with the direct method (DM). The "pseudo-analytical" solution $1 - \frac{\partial r^0(R,t)}{\partial R}$ is also plotted.

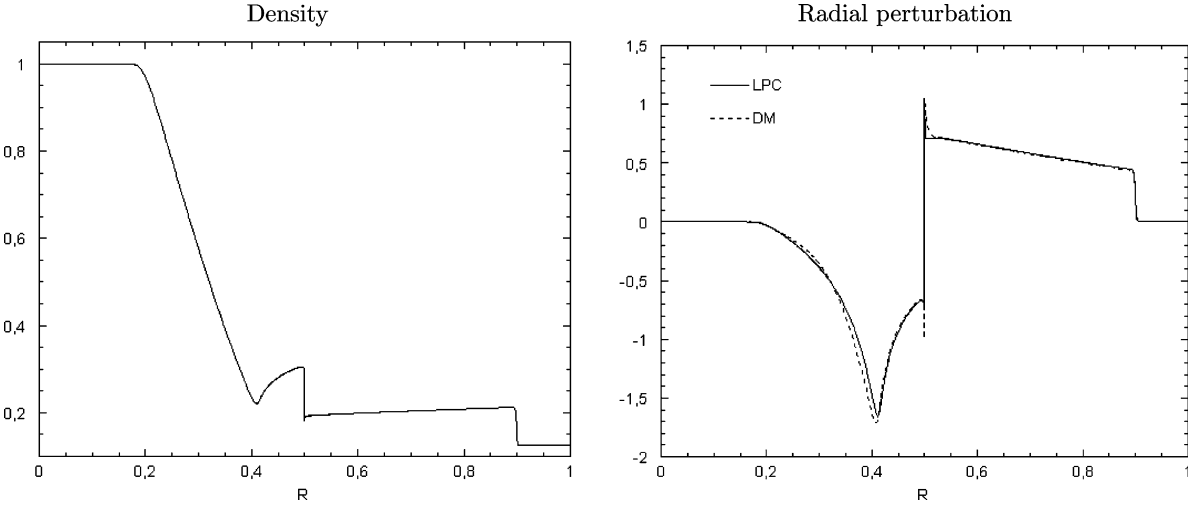

Fig. 3. Monodimensional perturbation in the spherical geometry at $t = 0.25$. Left: unperturbed density profile $\rho(R,t)$. Right: comparison of the radial perturbation obtained with the LPC code and with the direct method (DM).

We see in Fig. 2(left) that on the left of the contact discontinuity ($R < R_{\text{int}}$), $r(R,t)$ increases more rapidly than the function $r = R$, so that $1 - \partial_R r^0(R,t) < 0$. On the contrary, for $R > R_{\text{int}}$, we have $r(R,t) \simeq \alpha R$ with $\alpha < 1$. Therefore, the linear perturbation is almost constant and positive. This is what Fig. 2(right) shows. In the spherical case, the situation is much more complex since a convergence effect appears (the perturbed solution is not a translation of the unperturbed one) and Remark 5 does not apply. Comparison of LPC results with DM ones is shown in Fig. 3.

In both cases, profiles for the radial perturbations are close. We also expect the radial position $r(R,t)$ to be continuous so that the radial perturbation is almost a function.[5] Here the overshoot (undershoot) at the

[5] This is not the case of $\tilde{U}(R,t)$ which is a measure (see [4,15]). In particular, Dirac masses appear on $\tilde{U}(R,t)$ wherever $U(R,t)$ is discontinuous.

interface is due to wall heating: the density of the basic flow is under-estimated at the interface and this results in these overshoot (undershoot) on the linear perturbation.

Remark 6. We have noticed that the DM approach is very sensitive to the numerical scheme used, especially when dealing with second order schemes. We can easily convince ourselves that small oscillations (typically of the order of ε) on the basic flow have a dramatic effect when computing $\frac{U^{\varepsilon}(R,t)-U(R,t)}{\varepsilon}$. In a recent paper, Zalesak et al. [49] have studied the limits of the DM approach. They show that second order schemes are a source of nondifferentiability of the numerical algorithms which can make this approach incompatible with the accurate modelling of small amplitude perturbations. Their conclusions argue for the LPC approach.

This test case shows that the LPC code gives quite the same results as those one obtain using a Direct method (even if a great care is needed for the latter). Nevertheless, when dealing with multi-dimensional perturbations, the DM becomes quite complex to use. We show on the two following test cases that the LPC works as well in this context.

4.2. Isentropic implosion of a perturbed shell

We consider here the case of an isentropic compression of a shell filled with a perfect gas initially at rest for which analytical solutions are available. Solutions for the basic flow have been described by Kidder [27], and analytical solutions for the perturbed flow can be found in [5]. Let index 1 (respectively 2) denote the different variables defined on the internal (respectively external) surface of the shell.

4.2.1. Analytical solution for the basic flow

The initial condition is given by:

$$\begin{cases} \rho(R,0) = \left(\frac{\rho_2^{\gamma-1}(R^2-R_1^2)+\rho_1^{\gamma-1}(R_2^2-R^2)}{R_2^2-R_1^2}\right)^{\frac{1}{\gamma-1}}, \\ u(R,0) = 0, \\ p(R,0) = p_2\left(\frac{\rho}{\rho_2}\right)^{\gamma}, \end{cases}$$

where $\gamma = \frac{5}{3}$ is the adiabatic exponent. Let $r(R,t)$ denote the radius of a fluid particle at time t such that that $r(R,0) = R$. We will also denote $r_1 = r(R_1,t)$ and $r_2 = r(R_2,t)$. For boundary conditions, a pressure law is imposed on both the internal and external surfaces:

$$p(r_1,t) = p_1 h(t)^{-3\gamma} \quad \text{and} \quad p_2(r_2,t) = p_2 h(t)^{-3\gamma},$$

where $h(t)$ is the self-similar motion law, *i.e.* $r(R,t) = Rh(t)$, and is defined by

$$h(t) = \sqrt{1-\frac{t^2}{t_c^2}} \quad \text{with} \quad t_c = \sqrt{\frac{1}{2\gamma}\frac{R_2^2-R_1^2}{\varepsilon_2-\varepsilon_1}},$$

t_c being the collapse time and ε the internal energy. The self-similar solution is therefore given by

$$\begin{cases} \rho(r,t) = \frac{1}{h(t)^3}\rho\left(\frac{r}{h(t)},0\right), \\ u(r,t) = -\frac{rt}{t_c^2 h(t)^2}, \\ p(r,t) = p_2\left(\frac{\rho(r,t)}{\rho_2}\right)^{\gamma}. \end{cases}$$

4.2.2. Analytical solution for the perturbed flow

The basic flow being defined, we now want to perturb the internal and external surfaces of the shell. Therefore, we assume that radial positions are slightly perturbed in accordance with the following law (l is the spherical harmonic degree):

$$\tilde{r}(R,0) = \alpha_l R^{l-1} + \beta_l R^{-l-2}, \quad \text{for } R_1 \leqslant R \leqslant R_2, \tag{51}$$

together with the boundary conditions $\tilde{r}(R_1,0)=\tilde{R}_1$ and $\tilde{r}(R_r,0)=\tilde{R}_2$. Other variables are zero, except the transverse displacement field, which is linked to $\tilde{r}(R,0)$ through Eq. (29). It is shown in [5] that the analytical solution for the radial displacement field is given by

$$\tilde{r}(r,t)=\alpha_l r^{l-1} g_1(t/t_c)+\beta_l r^{-l-2} g_2(t/t_c),$$

with

$$\begin{cases} g_1(t)=\frac{1}{2}\sqrt{1-t^2}\left[\left(\frac{1-t}{1+t}\right)^{\frac{\sqrt{l}}{2}}+\left(\frac{1+t}{1-t}\right)^{\frac{\sqrt{l}}{2}}\right], \\ g_2(t)=\sqrt{1-t^2}\cos\left[\frac{\sqrt{l+1}}{2}\ln\left(\frac{1-t}{1+t}\right)\right]. \end{cases}$$

4.2.3. Numerical results

For the numerical simulations we have chosen $R_1=0.9, R_2=1, p_1=10^6, p_2=10^8$ and $\rho_2=10^{-4}$. From the isentropic condition $p_1\tau_1^\gamma=p_2\tau_2^\gamma$ we get the initial value for ρ_1.

Remark 7. The experimental order of convergence in space of the second order accurate scheme (49) and (50) has been measured on this test case at time $t=0.5t_c$. It is given in Table 1. Second order in space is almost achieved.

Now, we present the results obtained for three kinds of perturbations. The domain has been divided in 1000 regular cells, so that converged results have been obtained, and the final time is $t_f=0.999t_c$. In the first case, the internal surface is not perturbed and we choose $(\tilde{R}_1,\tilde{R}_2)=(0,1)$. Perturbation amplifications at the internal and external surfaces computed with the Linear Perturbation Code (LPC) presented here are compared with the analytical solutions for the mode numbers $l=4$ in Fig. 4 and $l=100$ in Fig. 5.

In the second and third cases, both surfaces are perturbed: $(\tilde{R}_1,\tilde{R}_2)=(1,0.55)$ and $(\tilde{R}_1,\tilde{R}_2)=(2.848738,1)$. For the initial condition $(\tilde{R}_1,\tilde{R}_2)=(1,0.55)$, comparisons of the perturbation amplifications at the internal and external surfaces are given in Fig. 6 for the mode number $l=4$ and in Fig. 7 for $l=100$, while for the initial condition $(\tilde{R}_1,\tilde{R}_2)=(2.848738,1)$ they are given in Fig. 8 for the mode number $l=8$. The effects of convergence are clearly seen on these figures. Indeed, since the acceleration is centripetal, the internal surface is Rayleigh–Taylor stable, but oscillating while the external surface is unstable. In a convergent geometry an aspect ratio effect is expected. This is retrieved here, and in the last case the external surface is even stabilized for $t<0.99t_c$. For all these test cases an excellent agreement between the computed and the analytical solutions is observed.

4.3. Richtmyer–Meshkov instability

This test case is devoted to the Richtmyer–Meshkov instability [37,32] for a spherically convergent/divergent flow. These instabilities occur when a shock wave collides with a perturbed interface separating two

Table 1
Experimental order of convergence (EOC) of the second order accurate scheme (49) and (50)

N	$\|\frac{\rho-\rho^{ex}}{\rho^{ex}}\|_1$	EOC	$\|\frac{r_1-r_1^{ex}}{r_1^{ex}}\|$	EOC	$\|\frac{r_2-r_2^{ex}}{r_2^{ex}}\|$	EOC
10	5.7349e−07	...	3.5459e−02	...	1.9195e−03	...
20	1.9611e−07	1.55	1.0403e−02	1.77	4.8663e−04	1.98
40	5.3986e−08	1.86	2.7979e−03	1.89	1.2890e−04	1.92
80	1.3927e−08	1.95	7.3404e−04	1.93	3.4413e−05	1.91
160	3.5015e−09	1.99	1.9200e−04	1.93	9.3150e−06	1.89
320	8.7337e−10	2.00	4.9600e−05	1.95	2.4800e−06	1.91
640	2.2309e−10	1.97	1.2021e−05	2.05	5.8562e−07	2.08
1280	5.5962e−11	1.99	3.0487e−06	1.98	1.4982e−07	1.97

N is the number of cells used in simulations.

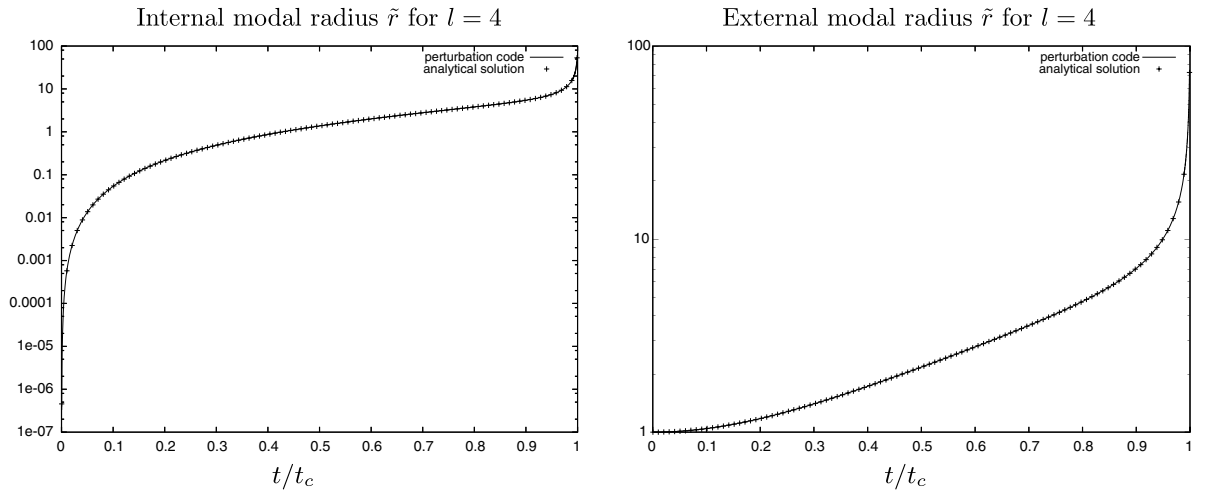

Fig. 4. Internal and external modal radii for the mode $l = 4$. Graphs are displayed using a logarithmic scale. Initial condition: $(\tilde{R}_1, \tilde{R}_2) = (0, 1)$.

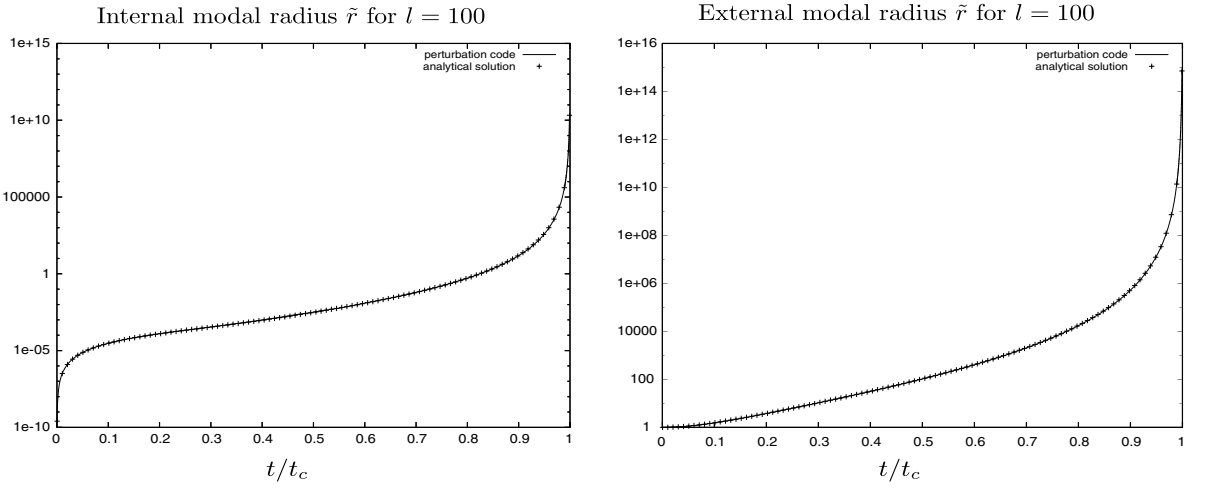

Fig. 5. Internal and external modal radii for the mode $l = 100$. Graphs are displayed using a logarithmic scale. Initial condition: $(\tilde{R}_1, \tilde{R}_2) = (0, 1)$.

different fluids. It has been widely studied in the planar case (see [45–47] and included references) and analytical solutions exist: for sufficiently small perturbations, the theory predicts that the amplitude of these perturbations grows linearly in time. This has been recovered using LPC in [9]. In a spherical geometry the situation is more complex, since convergence effects (referred as Bell–Plesset effects [14]) play an important role in the development of the instability. As a consequence analytical solutions are not yet available, except in very particular cases (see the work of Mikaelian [33] in the case of incompressible fluids) and the problem has to be investigated numerically (see for instance [13] and included references). For this test case, results are compared to 2D axisymmetric direct numerical simulations performed with the AMR Eulerian code Hera (for an overview of the features of this platform we refer the reader to [26]): the multi-fluid Euler equations are solved on a cartesian mesh (r, z) using a Lagrange + remap scheme[6] together with an alternate direction splitting. In the

[6] After a Lagrangian step, quantities are projected back onto the fixed Eulerian grid (see [17] pp. 192–195 for the description of such a method).

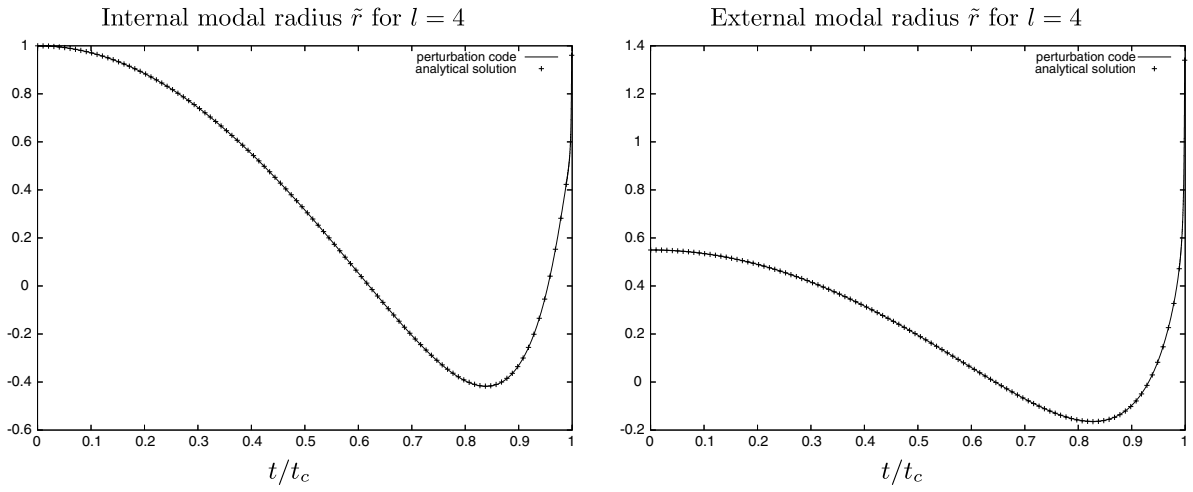

Fig. 6. Internal and external modal radii for the mode $l = 4$. Initial condition: $(\tilde{R}_1, \tilde{R}_2) = (1, 0.55)$.

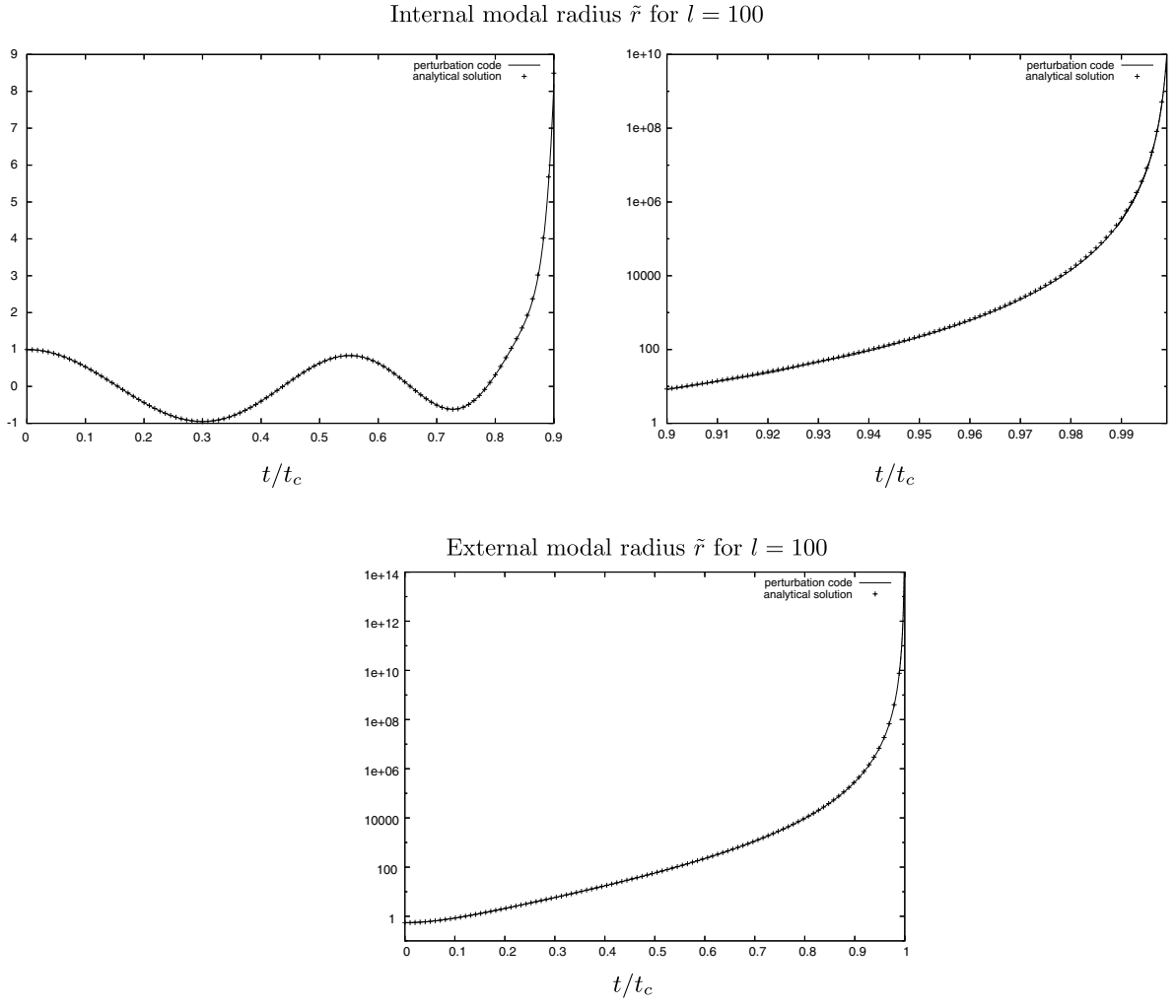

Fig. 7. Internal and external modal radii for the mode $l = 100$. Graphs displayed on top right and bottom are displayed using a logarithmic scale. Initial condition: $(\tilde{R}_1, \tilde{R}_2) = (1, 0.55)$.

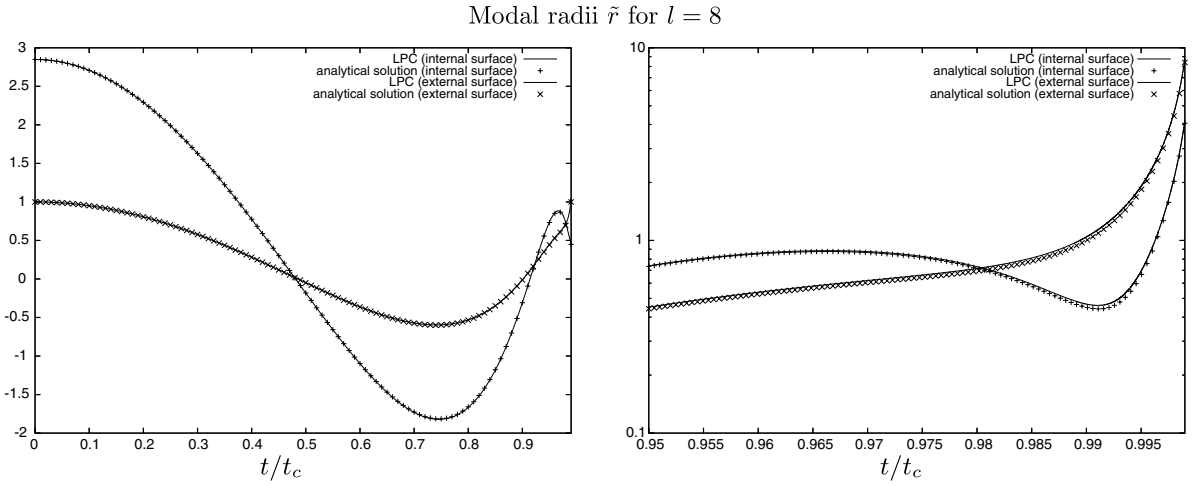

Fig. 8. Internal and external modal radii for the mode $l = 8$. Graph displayed on right is displayed using a logarithmic scale. Initial condition: $(\tilde{R}_1, \tilde{R}_2) = (2.848738, 1)$.

r-direction (respectively, z-direction), the scheme used in the Lagrangian phase is the one described in Section 3.1 with $\mathscr{A} = r$ (respectively, $\mathscr{A} = 1$) together with the second order TVD solver proposed in Section 3.3. For mixed cells this scheme is applied on global quantities and a subzonal model (in the spirit of [1]) is used to update partial ones. For the remapping phase a Youngs' interface reconstruction algorithm [48] is applied.

4.3.1. Initial conditions

Initial conditions for the LPC. Initial conditions for the basic flow are defined by

$$U_0^0(R) = \begin{cases} U_e^s & \text{if } 4 < R < 10, \\ U_e^u & \text{if } R_i < R < 4, \\ U_i & \text{if } 0 < R < R_i. \end{cases}$$

The interface between the internal sphere and the external shell is located at $R_i = 3$, while a shock, located at $R = 4$ is propagating in the external shell towards the center. Both fluids are governed by perfect gas laws whose adiabatic exponents are $\gamma_i = 3$ and $\gamma_e = 1.5$. The states U_e^u and U_i are given by

$$U_e^u = \begin{cases} \rho_e^u = 1, \\ u_e^u = 0, \\ p_e^u = 1, \end{cases} \quad U_i = \begin{cases} \rho_i = 4, \\ u_i = 0, \\ p_i = 1. \end{cases}$$

We denote by s the strength of the incident shock, defined by $s = 1 - \frac{p_e^u}{p_e^s}$. Once this parameter is specified, we easily determine the shocked state U_e^s using the Rankine–Hugoniot jump conditions. In the present application $s = 0.5$, so that the Mach number is approximately equal to 1.35.

Initial conditions for the linearized flow are $\tilde{U}_0(R) = 0$ and

$$\tilde{r}(R, 0) = \exp(-10|R - R_i|^2).$$

The transverse displacement field, which is linked to $\tilde{r}_0(R)$ through Eq. (29) is given by

$$\tilde{\Lambda}_{0,j} = -\rho_{0,j} \frac{(\mathscr{A}\tilde{r})_{0,j+\frac{1}{2}} - (\mathscr{A}\tilde{r})_{0,j-\frac{1}{2}}}{\Delta m_j}.$$

Such initial values for the perturbed flow correspond to a geometrically perturbed material contact discontinuity as it was explained in [9].

Initial conditions for the 2D axisymmetric simulation. For the 2D axisymmetric simulation, the basic flow is also given by the same states, but the interface between U_i and U_e^u is slightly perturbed by a Legendre mode number l of amplitude a_l^0:

$$R_i^{\varepsilon}(\theta,0) = R_i + a_l^0 P_l(\cos\theta),$$

where P_l is the Legendre polynomial of degree l and Θ the angle between the radial direction and the symmetry axis. Knowing the equation of the interface the code is able to compute the volume fraction of each fluid in mixed cells. Here $a_l^0 = 0.2$ has been chosen.

Remark 8. In order to compare LPC and Hera results, we must make sure that in the 2D simulations we stay in the linear regime and that results are independent of the initial value a_l^0. Generally (see [20] for instance), instabilities are considered to evolve linearly in time if

$$a_l^0 < 0.1\lambda \quad \text{with } \lambda \simeq 2\pi\frac{R_i}{l} \text{ the wavelength of the perturbation.} \tag{52}$$

As it is shown in [49], from a numerical point of view this criterion is not sufficient when investigating linear growth rates throughout 2D direct simulations. Indeed, *pure* single mode computations are not possible to handle with such tools and noninitialized modes necessarily appear (they may be seeded by round off errors for instance). Since the flow is intrinsically unstable these are not damped and mode coupling may occur. For these reasons, the instability will be considered in its linear regime if the amplitude of the noninitialized modes $a_{m\neq l}(t)$ always remains lower than the amplitude $a_l(t)$. We will also check that once this criterion is satisfied, results are independent of the choice of a_l^0.

4.3.2. Numerical results

For the LPC code, 2000 cells have been used and converged results have been obtained for all mode numbers less than 100, while in the 2D calculations, a 1280×640 mesh of level 0 has been used on a half sphere. The domain $R < 4$ is refined by a factor 3 so that this would lead to 7,372,800 cells without AMR. With such a mesh quasi-converged results are obtained for sufficiently low mode numbers (for $l \leqslant 20$).

The interface radius and velocity versus time are given in Fig. 9. At $t \simeq 0.6$ the interface is impulsively accelerated by the incident shock. Contrarily to the planar case, after the shock interaction, the interface velocity is not constant but increases. This is due to the convergent symmetry. At $t \simeq 2.1$ the convergent shock is reflected at the center and a divergent shock propagates in the internal sphere. It interacts a second time at $t \simeq 2.9$ with the interface. This gives rise to second transmitted and reflected waves.

An unperturbed simulation has also been performed in order to compare the basic flows computed by both methods. A very good agreement is observed in Fig. 10(left) where density profiles at three different times are represented. Two dimensional perturbed density plots are also given in this figure (right) for the Legendre mode number $l = 10$.

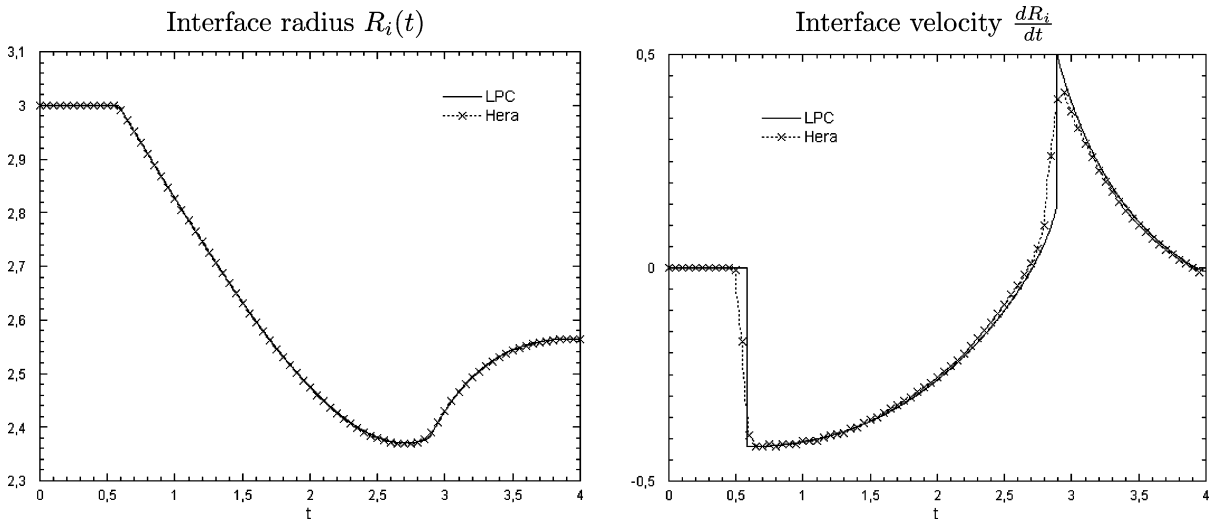

Fig. 9. Richtmyer–Meshkov instability. Left: interface radius versus time. Right: interface velocity versus time.

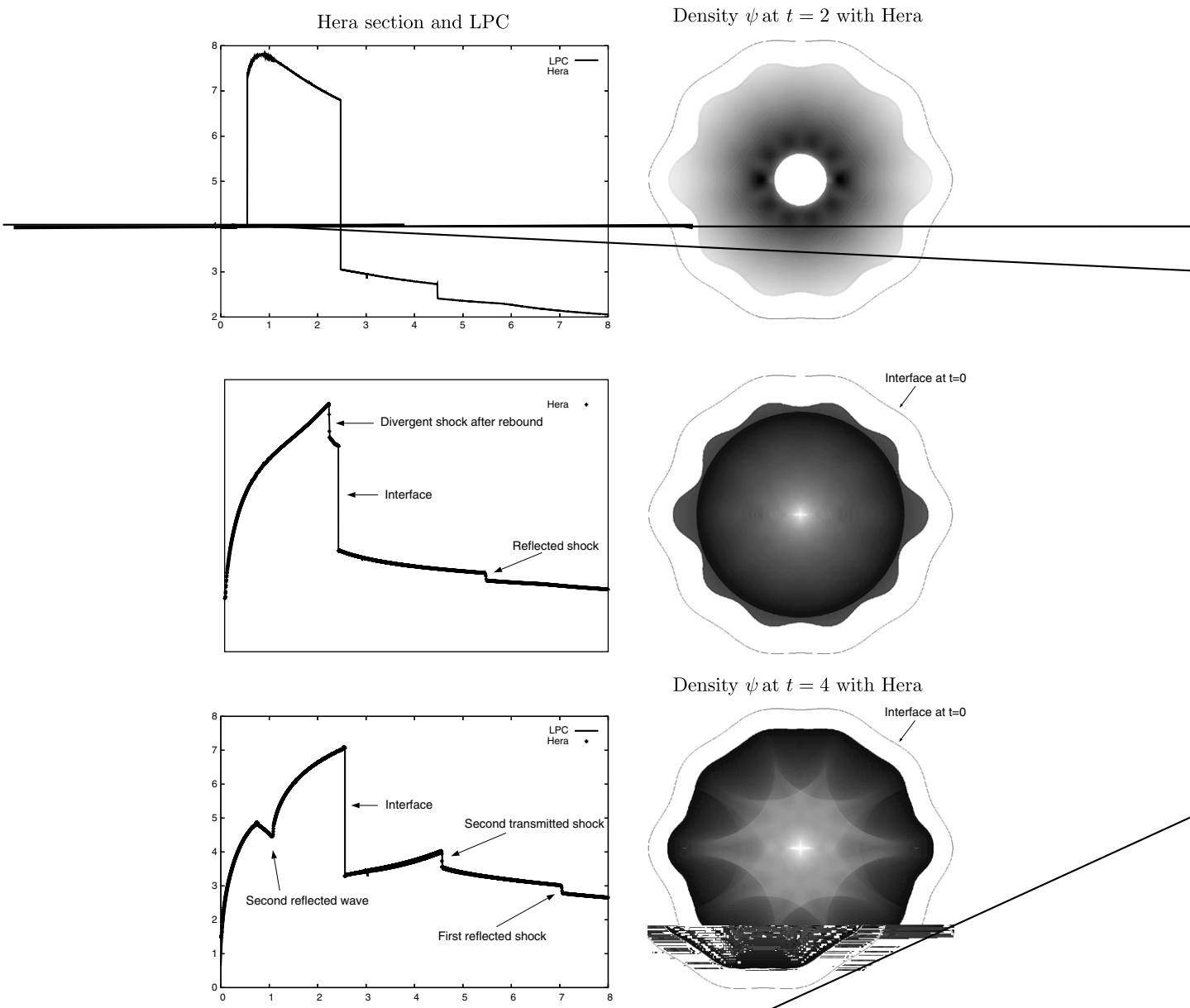

Fig. 10. Richtmyer–Meshkov instability. Density profiles at $t = 2$ (top), $t = 2.8$ (middle) and $t = 4$ (bottom). On the left, a Hera section of the unperturbed 2D simulation compared to the basic flow computed with the LPC. On the right, results obtained with the 2D AMR Eulerian code Hera for the Legendre mode number $l = 10$. Only the internal sphere is plotted, together with the initial interface profile.

In the 2D simulations, thanks to the Youngs' interface reconstruction, the interface $R_i^\varepsilon(\theta, t)$ can be numerically tracked and post-processed. Since

$$R_i^\varepsilon(\theta, t) = \sum_{m=0}^{\infty} a_m(t) P_m(\cos\theta),$$

using the orthogonality property of the Legendre polynomials [6] one gets

$$a_l(t) = \frac{2l+1}{2} \int_{-1}^{1} R_i^\varepsilon(\theta, t) P_l(\cos\theta) d(\cos\theta).$$

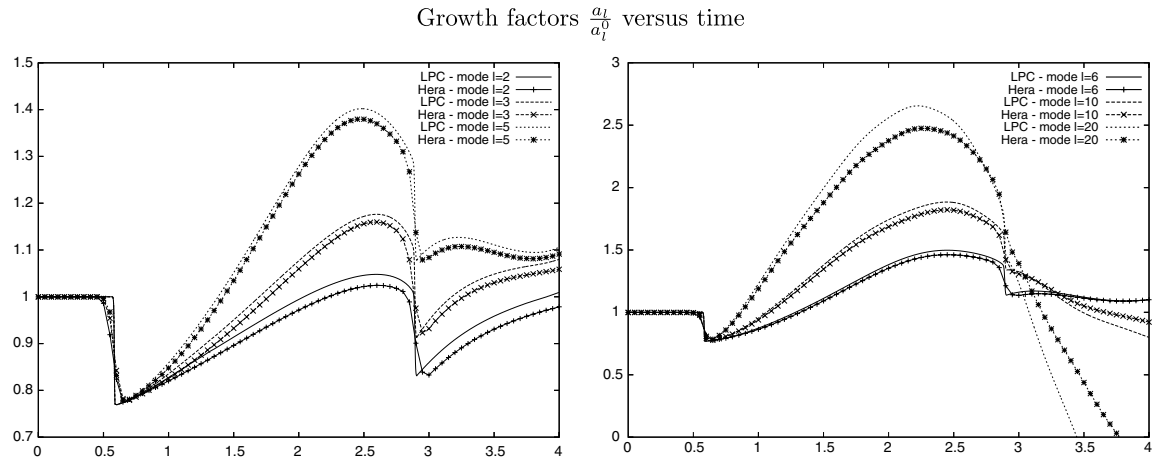

Fig. 11. Richtmyer–Meshkov instability. Comparison of the growth factors $\frac{a_l}{a_l^0}$ versus time obtained with both methods (LPC and 2D Hera).

The amplitude of each mode is therefore recovered by evaluating this integral. As was said in Remark 8, we checked that the amplitude of the noninitialized modes $a_{m\neq l}(t)$ always remain lower than the amplitude $a_l(t)$ so that the instability can be considered in its linear regime. We can therefore compare the growth factors $\frac{a_l}{a_l^0}$ obtained by both methods (for the LPC approach, it is simply defined by $\tilde{r}(R_i,t)$). This is done in Fig. 11 for Legendre mode numbers $l = 2, 3, 5, 6, 10$ and 20. Before the shock front hits the interface (which happens at $t \simeq 0.6$), the growth factor of the perturbation remains constant. When this front interacts with this interface, its theoretical value is $(1 - \Delta u/\sigma)$ (see [45] for instance), where Σ is the Eulerian speed of the incident shock wave and Δu the velocity jump of the interface due to the shock interaction. Then the amplitude of the perturbation grows. In a planar geometry and for an infinite domain, it theorically grows linearly. This is almost the case right after the interaction, but convergence effects (known as Bell–Plesset effects [14]) rapidly reduce the growth factor. This one begins to decrease before the interface undergoes a new shock interaction (divergent shock coming from the center) at $t \simeq 2.9$. A phase inversion (which corresponds to negative growth factors) is even seen for high mode numbers (here for $l = 20$). We observe a good agreement between both approaches, especially for low mode numbers. We have also observed that the more we refine the 2D mesh, closer to the (converged) 1D linear perturbation results we are.

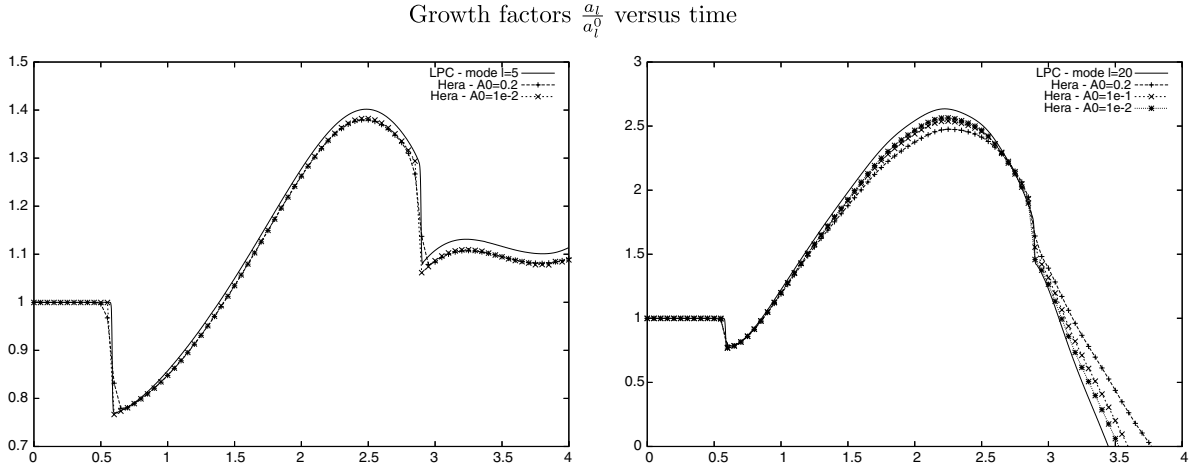

Fig. 12. Richtmyer–Meshkov instability. Comparison of the growth factors $\frac{a_l}{a_l^0}$ versus time obtained with Hera for different values of a_l^0. Left: mode $l = 5$ with $a_l^0 = 0.2$ and $a_l^0 = 10^{-2}$. Right: mode $l = 20$ with $a_l^0 = 0.2$, $a_l^0 = 10^{-2}$ and $a_l^0 = 10^{-3}$. LPC results are also plotted.

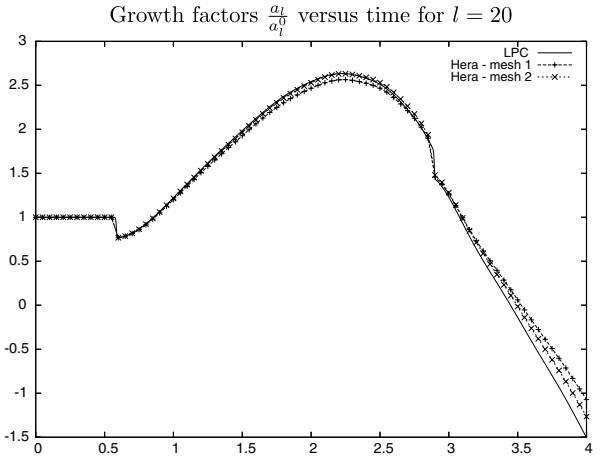

Fig. 13. Richtmyer–Meshkov instability. Comparison of the growth factors $\frac{a_l}{a_l^0}$ versus time for $l = 20$ and $a_l^0 = 10^{-2}$ obtained with Hera on two different meshes. Mesh 1: 1280×640, mesh 2: 2560×1280. For both meshes, the domain $R < 4$ is refined by a factor 3. LPC results are also plotted.

As was said in Remark 8, we have checked that Hera results were independent of the initial amplitude a_l^0 (provided $a_l^0 \leqslant 0.2$) for sufficiently small mode numbers (here $l \leqslant 10$). This can be seen in Fig. 12(left) where results obtained with $a_l^0 = 0.2$ and $a_l^0 = 10^{-2}$ for $l = 5$ are compared. As l increases, the initial value $a_l^0 = 0.2$ begins to be too great (for $l > 10$ the heuristic criterion (52) is not satisfied). This is one of the reasons why differences observed in Fig. 11 are more important for $l = 20$ than for smaller mode numbers. Indeed, choosing a smaller value of a_l^0 reduces the discrepancies between both approaches (see Fig. 12(right) where results obtained with $a_l^0 = 0.2$, $a_l^0 = 10^{-1}$ and $a_l^0 = 10^{-2}$ for $l = 20$ are plotted). Another reason is that 2D results are not *converged* for such mode numbers: the more l increases, the more the mesh needs to be refined. The same computation has been done for $l = 20$ and $a_l^0 = 10^{-2}$ on the preceding mesh (referenced mesh) refined by a factor 2 (without AMR this would lead to 29,491,200 cells). Results are plotted in Fig. 13 where an excellent agreement between both approaches is observed. This study shows that 2D direct computations must be handled with a great care and that they can rapidly become very expensive (the refined computation – on mesh 2 – lasts about 5 h on 128 cpu).

The interest of the linear perturbation approach for such studies becomes very clear: converged results are produced in a very efficient manner (a run lasts less than 1 min on a standard PC here) while avoiding the accuracy limitations faced by 2D direct computations when dealing with perturbations of small relative amplitudes.

5. Conclusion

A purely Lagrangian method dedicated to linear perturbation studies about 1D spherically symmetric flows governed by the gas dynamics equations has been described. The structure of multi-dimensional systems which extends results of Després et al. [11,12] in spherical coordinates has been fully exploited. It is shown that within this formulation, systems satisfied by the basic and the perturbed flows as well as accurate and robust numerical schemes may be produced in a straightforward manner. Beyond these advantages, the main interest of this approach lies in the fact that principles involved here immediately apply to many fluid models with zero entropy flux such as plasma two-temperature hydrodynamics equations [25], ideal magnetohydrodynamics [3], certain models of radiation hydrodynamics, elasto-plasticity, etc. Showing that this linear perturbation approach works in the simple, yet demanding, gas dynamics context indicates that it may also apply to more sophisticated fluid models.

Through our experience [24,9] and the presented numerical results, it appears that this method is well suited for handling geometrically perturbed material interfaces separating fluids (eventually governed by different equations of state). It is a very efficient alternative to 2D/3D calculations (these latter having to be very carefully

used for such studies [49]). The scheme numerical capabilities have been illustrated on three test cases of increasing difficulty. In the last one it is shown that with such a tool one is able to compute accurately the growth rates of a small interface perturbation, subject to spherical Richtmyer–Meshkov instabilities, a difficult situation to treat analytically since the basic flow is highly unsteady and convergence as well as compressibility effects are important. We also saw through this test case that multi-dimensional calculations could rapidly become very expensive. In fact both approaches are complementary: linear perturbation computations are restricted to linear stability analysis while multi-dimensional calculations are mandatory for rendering nonlinear effects.

This approach has also been applied in the ICF context. To do so, a nonlinear diffusion operator has been added, together with its linearized version. A systematic comparison of results obtained with the LPC and a direct Lagrangian method has been carried out and has produced very convincing results for the growth rates of the fuel/shell interface instability in the deceleration phase [43].

Acknowledgments

Author gratefully thanks H. Jourdren and B. Després for valuable discussions.

Appendix A. Proofs

A.1. Proof of Proposition 1

The proof of this proposition just uses the chain rule and the following:

Lemma 3. *Let* $(t,r,\theta,\phi) \to (t,R,\Theta,\Phi)$ *be defined by* (3). *Therefore*,

$$\nabla_{(r,\theta,\phi)} T = |J|^{-1} \tilde{J} \nabla_{(R,\Theta,\Phi)} T, \tag{53}$$

where J *is defined by* (5) *and* $\tilde{J}$ *by* (8).

This result is straight forward since

$$\nabla_{(r,\theta,\phi)} T = \left[\frac{\partial(R,\Theta,\Phi)}{\partial(r,\theta,\phi)}\right]^t \nabla_{(R,\Theta,\Phi)} T, = (J^{-1})^t \nabla_{(R,\Theta,\Phi)} T,$$

and $J^{-1} = |J|^{-1}\tilde{J}^t$. A noteworthy property of this comatrix is that $\nabla \cdot \tilde{J} = 0$. This can be easily seen using the definition of the jacobian matrix components and crossed derivatives.

Using definition (7) of the jacobian, we have

$$\begin{aligned}
\partial_{t_{|R,\Theta,\Phi}} |J| &= -\frac{|J|}{\rho r^2 \sin\theta} \partial_{t_{|R,\Theta,\Phi}} (\rho r^2 \sin\theta), \\
&= -\frac{|J|}{\rho r^2 \sin\theta} \left[\partial_t(\rho r^2 \sin\theta) + u_r \partial_r(\rho r^2 \sin\theta) + u_\theta \partial_\theta(\rho r \sin\theta) + u_\phi \partial_\phi(\rho r)\right], \\
&= |J| \left[\partial_r u_r + \frac{1}{r}\partial_\theta u_\theta + \frac{1}{r\sin\theta}\partial_\phi u_\phi\right], = |J| \nabla_{(r,\theta,\phi)} \cdot \mathbf{v},
\end{aligned}$$

where we have used (9) and the mass conservation equation (12a). Therefore,

$$\begin{aligned}
\partial_{t_{|R,\Theta,\Phi}} (|J|a) &= a\partial_{t_{|R,\Theta,\Phi}} |J| + |J| \partial_{t_{|R,\Theta,\Phi}} a, = |J| a \nabla_{(r,\theta,\phi)} \cdot \mathbf{v} + |J| \left[\partial_t a + u_r \partial_r a + \frac{u_\theta}{r}\partial_\theta a + \frac{u_\phi}{r\sin\theta}\partial_\phi a\right], \\
&= -|J| \nabla_{(r,\theta,\phi)} \cdot (\mathbf{f} - a\mathbf{v}) + |J| s,
\end{aligned}$$

Applying (53) to this equation together with the fact that $\nabla \cdot \tilde{J} = 0$ gives the desired result.

A.2. Proof of Proposition 2

The result is immediate since it only requires the application of Proposition 1 to system (12a), except for the mass conservation equation, where it is applied on the trivial equation $\partial_t(r^2 \sin\theta) = 0$. Let us see on the second equation of (12a) how calculations work. We have

$$\begin{cases} a = r^2 \sin\theta \cdot \rho u_r, \\ \mathbf{f} = (r^2 \sin\theta \cdot (\rho u_r^2 + p), r\sin\theta \cdot \rho u_\theta, r \cdot \rho u_\phi)^t, \end{cases}$$

so that

$$\mathbf{f} - a\mathbf{v} = (r^2 \sin\theta \cdot p, 0, 0)^t.$$

Using (7), (11) and the conventional notation $(R, \Theta, \Phi) = (1, 2, 3)$ we get

$$\rho_0 R^2 \sin\Theta \partial_t u_r + \sum_{i=R,\Theta,\Phi} \partial_i (r^2 \sin\theta J_{i1}.p) = |J| s_r.$$

Performing same calculations on the other equations and introducing the reduced entropic variables Ψ and the matrix $\mathcal{N}$ yields to the result.

A.3. Proof of the divergence constraint (15)

We only prove this property for the first component on the second line. Computations for other components work rigourously on the same template. We have to prove that

$$\mathcal{Q} = \partial_R(r^2 \sin\theta(FN - MG)) + \partial_\Theta(-r^2 \sin\theta(BN - CM)) + \partial_\Phi(r^2 \sin\theta(BG - CF)) - 2r\sin\theta|J| = 0.$$

Using the fact that $\nabla \cdot \tilde{J} = 0$ where $\tilde{J}$ is defined by (8), we get

$$\begin{aligned} \mathcal{Q} &= (FN - MG)\partial_R(r^2\sin\theta) - (BN - CM)\partial_\Theta(r^2\sin\theta) + (BG - CF)\partial_\Phi(r^2\sin\theta) - 2r\sin\theta|J|, \\ &= [(FN - MG)\partial_R r - (BN - CM)\partial_\Theta r + (BG - CF)\partial_\Phi r - |J|]2r\sin\theta \\ &\quad + [(FN - MG)\partial_R\theta - (BN - CM)\partial_\Theta\theta + (BG - CF)\partial_\Phi\theta]r^2\cos\theta. \end{aligned}$$

These two terms are zero thanks to (5).

References

[1] D.J. Benson, Computational methods in Lagrangian and Eulerian hydrocodes, Comp. Meth. Appl. Mech. Eng. 99 (1992) 235–394.
[2] R. Betti, N. Goncharov, R.L. McCrory, C.P. Verdon, Growth rates of the ablative Rayleigh–Taylor instability in inertial confinement fusion, Phys. Plasmas 5 (5) (1998) 1446–1454.
[3] F. Bézard, B. Després, An entropic solver for ideal lagrangian magnetohydrodynamics, J. Comp. Phys. 154 (1999) 65–89.
[4] F. Bouchut, F. James, One-dimensional transport equations with discontinuous coefficients, Nonlinear Anal., TMA 32 (7) (1998) 891–933.
[5] J. Breil, L. Hallo, P.-H. Maire, M. Olazabal-Loumé, Hydrodynamic instabilities in axisymmetric geometry self-similar models and numerical simulations, Laser Part. Beams 23 (2005) 155–160.
[6] I.N. Bronshtein, K.A. Semendyayev, G. Musiol, H. Muehlig, Handbook of Mathematics, fourth english ed., Springer, 2004.
[7] L. Brun, B. Sitt, Approche lagrangienne du problème des instabilités hydrodynamiques d'une implosion à symétrie plane ou sphérique, Technical Report CEA-R-5012, CEA, 1979 (in French).
[8] V.Ya. Bukharova, G.A. Grishina, O.M. Zotova, T.G. Ivtchenko, Linearization of the multi-dimensional equations of gas dynamics with heat conduction in Lagrangian variables, VANT, Ser. Met. i progr. chisl. resh. zad. mat. fiziki 2 (4) (1979) 6–11 (in Russian).
[9] J.-M. Clarisse, S. Jaouen, P.-A. Raviart, A Godunov-type method in Lagrangian coordinates for computing linearly-perturbed planar-symmetric flows of gas dynamics, J. Comp. Phys. 198 (2004) 80–105.
[10] R. Dautray, J.-P. Watteau, La fusion thermonucléaire inertielle par laser. La fusion par confinement inertiel, Eyrolles, 1993.
[11] B. Després, Lagrangian systems of conservation laws. Invariance properties of Lagrangian systems of conservation laws, approximate Riemann solvers and the entropy condition, Numer. Math. 89 (2001) 99–134.
[12] B. Després, C. Mazeran, Lagrangian gas dynamics in two dimensions and Lagrangian systems, Arch. Ration. Mech. Anal. 178 (2005) 327–372.
[13] S. Dutta, J. Glimm, J.W. Grove, D.H. Sharp, Y. Zhang, Spherical Richtmyer–Meshkov instability for axysymmetric flow, Math. Comp. Simul. 65 (2004) 417–430.
[14] R. Epstein, On the Bell–Plesset effects: the effects of uniform compression and geometrical convergence on the classical Rayleigh–Taylor instability, Phys. Plasmas 11 (2004) 5114–5124.
[15] E. Godlewski, M. Olazabal, P.-A. Raviart, On the linearization of hyperbolic systems of conservation laws. Application to stability, in: Equations aux dérivées partielles et applications, articles dédiés à J.-L. Lions, Gauthier-Villars, Paris, 1998, pp. 549–570.
[16] E. Godlewski, M. Olazabal, P.-A. Raviart, On the linearization of systems of conservation laws for fluids at a material contact discontinuity, J. Math. Pures Appl. 78 (1999) 1013–1042.

[17] E. Godlewski, P.-A. Raviart, Numerical approximation of hyperbolic systems of conservation laws, Applied Mathematical Sciences, vol. 118, Springer-Verlag, 1996.
[18] E. Godlewski, P.-A. Raviart, The linearized stability of solutions of nonlinear hyperbolic systems of conservation laws. A general numerical approach, Math. Comp. Simul. 50 (1999) 77–95.
[19] G.A. Grishina, Linear approximation method in gas dynamics problem numerical computations, Technical Report 121, USSR Academy of Sciences IAM, 1980 (in Russian).
[20] S.W. Haan, Onset of nonlinear saturation for Rayleigh–Taylor growth in the presence of a full spectrum of modes, Phys. Rev. A 39 (11) (1989) 5812–5825.
[21] D.B. Henderson, R.L. Morse, Symmetry of laser-driven implosions, Phys. Rev. Lett. 32 (7) (1974) 355–358.
[22] W.H. Hui, S. Kudriakov, A unified coordinate system for solving the three-dimensional Euler equations, J. Comp. Phys. 172 (2001) 235–260.
[23] W.H. Hui, P.Y. Li, Z.W. Li, A unified coordinate system for solving the two-dimensional Euler equations, J. Comp. Phys. 153 (1999) 596–637.
[24] S. Jaouen, Étude mathématique et numérique de stabilité pour des modèles hydrodynamiques avec transition de phase, Thèse de doctorat, Université Paris 6, 2001.
[25] S. Jaouen, B. Després, Solveur entropique d'ordre élevé pour les équations de l'hydrodynamique à deux températures, Stage de DEA, CEA-Université de Bordeaux I, 1997 (in French).
[26] H. Jourdren, HERA: a hydrodynamic AMR platform for multi-physics simulations, in: Plewa Tomasz, et al. (Eds.), Adaptative Mesh Refinement – Theory and Applications, Proceedings of the Chicago Workshop on Adaptative Mesh Refinement Methods, Chicago, IL, USA, September 3–5, 2003, Lecture Notes in Computational Science and Engineering, vol. 41. Springer, Berlin, 2005, pp. 283–294.
[27] R.E. Kidder, Laser-driven compression of hollow shells: power requirements and stability limitations, Nuclear Fusion 1 (1976) 3–14.
[28] H.J. Kull, S.I. Anisimov, Ablative stabilization in the incompressible Rayleigh–Taylor instability, Phys. Fluids 29 (7) (1986) 2067–2075.
[29] P. Lax, B. Wendroff, Systems of conservation laws, Commun. Pure Appl. Math. 13 (1960) 217–237.
[30] J.D. Lindl, Inertial Confinement Fusion, Springer, New York, 1998.
[31] R.L. McCrory, R.L. Morse, K.A. Taggart, Growth and saturation of instability of spherical implosions driven by laser or charged particle beams, Nucl. Sci. Eng. 64 (1977) 163–176.
[32] E.E. Meshkov, Instability of the interface of two gases accelerated by a shock wave, Sov. Fluid Dyn. 4 (1969) 101–104.
[33] K.O. Mikaelian, Rayleigh–Taylor and Richtmyer–Meshkov instabilities and mixing in stratified spherical shells, Phys. Rev. A. 42 (6) (1990) 3400–3420.
[34] C.D. Munz, On Godunov-type schemes for Lagrangian gas dynamics, SIAM J. Numer. Anal. 31 (1) (1994) 17–42.
[35] M. Olazabal, Modélisation numérique de problèmes de stabilité linéarisée. Application aux équations de la dynamique des gaz et de la MHD idéale, Thèse de doctorat, Université Paris 6, 1998.
[36] Lord Rayleigh, Investigation of the character of the equilibrium of an incompressible heavy fluid of variable density, Proc. Lond. Math. Soc. 14 (1900) 170–177.
[37] R.D. Richtmyer, Taylor instability in shock acceleration of compressible fluids, Commun. Pure Appl. Math. 13 (1960) 297–319.
[38] R.D. Richtmyer, K.W. Morton, Difference Methods for Initial-value Problems, second ed., Wiley-Interscience, 1967.
[39] J. Sanz, R. Betti, Analytical model of the ablative Rayleigh–Taylor instability in the deceleration phase, Phys. Plasmas 12 (2005) 042704.
[40] A.J. Scannapieco, C.W. Cranfill, A derivation of the physical equations solved in the inertial confinement stability code DOC, Technical Report LA-7214-MS, Los Alamos Scientific Laboratory, 1978.
[41] H. Takabe, K. Mima, L. Montierth, R.L. Morse, Self-consistent growth rate of the Rayleigh–Taylor instability in an ablatively accelerating plasma, Phys. Fluids 28 (1985) 3676–3682.
[42] G.I. Taylor, The instability of liquid surfaces when accelerated in a direction perpendicular to their planes, Proc. Lond. Math. Soc. 201 (1950) 1092–1096.
[43] M. Temporal, S. Jaouen, L. Masse, B. Canaud, Hydrodynamic instabilities in ablative tamped flows, Phys. Plasmas 13 (2006) 122701.
[44] E.F. Toro, Riemann Solvers and Numerical Methods for Fluid Dynamics: A Practical Introduction, second ed., Springer, Berlin, 1999.
[45] M. Vandenboomgaerde, C. Mügler, S. Gauthier, Impulsive model for the Richtmyer–Meshkov instability, Phys. Rev. E 58 (2) (1998) 1874–1882.
[46] J.G. Wouchuk, Growth rate of the Richtmyer–Meshkov instability when a rarefaction is reflected, Phys. Plasmas 8 (6) (2001) 2890–2907.
[47] Y. Yang, Q. Zhang, D.H. Sharp, Small amplitude theory of Richtmyer–Meshkov instability, Phys. Fluids 6 (5) (1994) 1856–1873.
[48] D. Youngs, An interface tracking method for a 3D Eulerian hydrodynamics code. Technical report, AWRE Design Mathematics Division, 1992. Report AWRE/44/92/35.
[49] S.T. Zalesak, A.J. Schmitt, A.L. Velikovich, J.H. Gardner, Modeling fluid instabilities in inertial confinement fusion hydrodynamics codes, Phys. Plasmas 12 (2005) 056311.